SATIF-15:
15th Workshop on Shielding aspects of Accelerators, Targets, and Irradiation Facilities

Facility for Rare Isotope Beams (FRIB) at Michigan State University
East Lansing, Michigan USA
20-23 September 2022.

Session 7: Source Terms / Medical Accelerators and Session 8: Radiation Damage / High Intensity Laser Facilities / Techniques & Applications

Table of contents

1. Measurement of neutron production yields of 345 MeV/u ^{238}U + Cu with a time-of-flight method

Kenta Sugihara[1,2*], Nobuhiro Shigyo[1,2], Atsuko Akashio[1], Kanenobu Tanaka[1]
[1]RIKEN Nishina Center, 2-1 Hirosawa, Wako, Saitama, 351-0198, Japan
[2]Kyushu University, Motooka, Nishi-ku, Fukuoka, 819-0395, Japan
[*]kenta.sugihara@kek.jp (Present address: KEK, 1-1 Oho, Tsukuba, Ibaraki, 305-0801, Japan)

Neutron energy spectra from 345 MeV/u ^{238}U incidence on a copper target was measured at 0˚, 45˚, and 90˚ with a time-of-flight technique. In order to confirm the prediction accuracy of nuclear reaction models implemented in Particle and Heavy Ion Transport code System and GEometry ANd Tracking 4, the measured data were compared with the two versions of JAERI Quantum Molecular Dynamics (JQMD) model with Generalized Evaporation Model (GEM), JQMD + statistical multi-fragmentation model + GEM, and the G4QMD + GEM. The best agreement within JQMD version 2 and the measured data was observed at 0˚.

1.1. Introduction

These days, a variety of applications of accelerators are widely spread, e.g., medicines with radioactive isotopes (RI) (Fujiki, 2019), nuclear physics (Ahn, 2019), and RI beam production (Suzuki, 2013). With obtaining RI beam with a wide range of mass number, the utilization of high-intensity uranium-238 (^{238}U) beam is adopted or planned, such as Facility for Rare Isotope Beams (Wei, 2019) in America, Facility for Antiproton and Ion Research (Augostin, 2018) in Germany, and Rare isotope accelerator complex for ON-line experiments (Kim, 2020) in Korea.

As one of such facilities also in Japan, Radioactive Isotope Beam Factory (RIBF) (Yano, 2007) at RIKEN provides ^{238}U beam, the energy of which is 345 MeV/u. The current operational and permitted intensity of the ^{238}U beam is 70 pnA and 300 pnA, respectively. Aiming at high-efficient RI beam production, a future improvement of the ^{238}U beam intensity is in progress. Because a number of neutrons are generated due to the reactions between the ^{238}U beam and a copper (Cu) beam dump, the optimization of a radiation shielding is indispensable. The shielding around the beam dump at RIBF (Uwamino, 2000) was originally designed by the Moyer model (Moyer, 1962) with estimating the source term from the neutron production thick target yields (TTYs) data of neon beam (Kurosawa, 2000). Due to the derivation, an uncertainty of the source term is still remained. Improvement of the performance for computers enabled us to estimate the source term by nuclear reaction models. The reaction induced by the ^{238}U beam is described by two versions of JAERI Quantum Molecular Dynamics (JQMD) (Niita, 1995) (Ogawa, 2015) followed by Generalized Evaporation Model (GEM) (Furihata, 2000) implemented in Particle and Heavy Ion Transport code System (PHITS) version 3.26 (Sato, 2018). In addition, Statistical Multi-fragmentation Model (SMM) (Ogawa, 2013) is also applied for more precise evaluation of pre-equilibrium process. Furthermore, G4QMD (Tatsumi, 2010) in GEometry ANd Tracking 4 (Geant4) version 10.6.p01. (Allison, 2016) is also utilized. However, the prediction accuracy of the models should be examined prior to applying the source term calculation. Therefore, benchmark study of the nuclear reaction models through the measurement of the TTY from 345 MeV/u ^{238}U incidence on Cu is absolutely desired at RIBF.

Measurement of the neutron production TTY from ^{238}U beam of 345 MeV/u on a copper target for 0˚, 45˚, and 90˚ with a time-of-flight technique was already completed (Sugihara, 2022). Thus, the purpose of this study is to obtain the benchmark of the JQMD version 1 + GEM (JQMD1/GEM), JQMD version 1 + SMM + GEM (JQMD1/SMM/GEM), JQMD version2 + GEM(JQMD2/GEM), and G4QMD + GEM to clarify the availability of these models.

1.2. Experiment

The detailed explanation of the experiment is given in a reference (Sugihara, 2022). The illustration of our experimental arrangement is shown in Figure 1.1.

The incident energy of the ^{238}U beam was 345 MeV/u. The intensity of the beam was 1 x 10^6 pps. The interval of the beam pulse was 54 nsec attributed to the radio frequency of accelerators. A Cu target with 10 mm thickness was located in the F10 vacuum chamber. The thickness was determined to be thicker than the range of the beam (3.3 mm).

Generated neutrons were measured by organic liquid scintillators placed at 0˚, 45˚, and 90˚. The flight path length for 0˚, 45˚, and 90˚ was 9.5, 4.0, and 4.0 m, respectively. The kinetic energy of neutrons was calculated with the use of a time-of-flight technique. The minimum energy of measurable neutrons for 0˚, 45˚, and 90˚ was about 130, 40, and 40 MeV, respectively, which was attributed to the interval of the beam pulse and the flight path length. Because the organic liquid scintillators were sensitive to not only neutrons but also charged particles. To eliminate charged particles' events, a plastic scintillator was placed in front of each neutron detector.

The contribution of the background neutrons was subtracted by a measurement with the 1-m-thick iron shadow bar.

Figure 1.1. Experimental arrangement of our experiment.
In this figure, "FPL" is Flight Path Length.

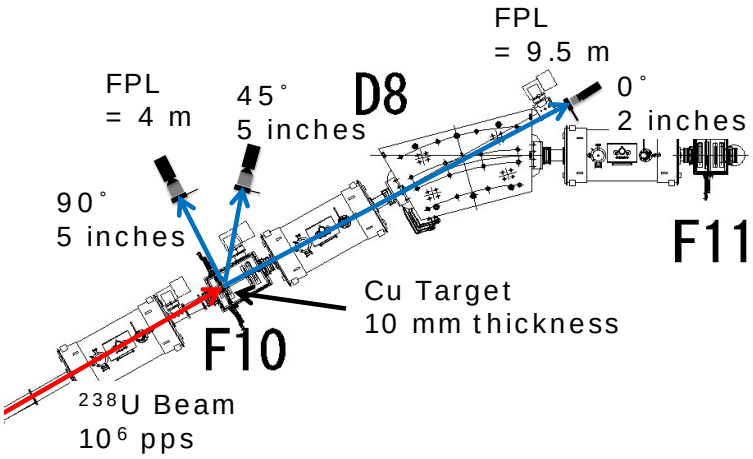

1.3. Result

Because the way of the analysis is introduced in a reference (Sugihara, 2022), we omit details of data analysis. The comparison of the neutron production TTYs via the reaction of 345 MeV/u ^{238}U + Cu among the measured data, JQMD1/GEM, JQMD2/GEM, JQMD1/SMM/GEM, and G4QMD/GEM is shown in Figure 1.2. The horizontal and

vertical axis stands for the neutron energy [MeV] and the TTYs [n/sr/MeV/source], respectively. Markers mean the measured data. The red, light-blue, pink, and green lines represent the results of JQMD1/GEM, JQMD2/GEM, JQMD1/SMM/GEM, and G4QMD/GEM, respectively.

Figure 1.2. Comparison among the measured data, JQMD1/GEM, JQMD2/GEM, JQMD1/SMM/GEM, and G4QMD/GEM.

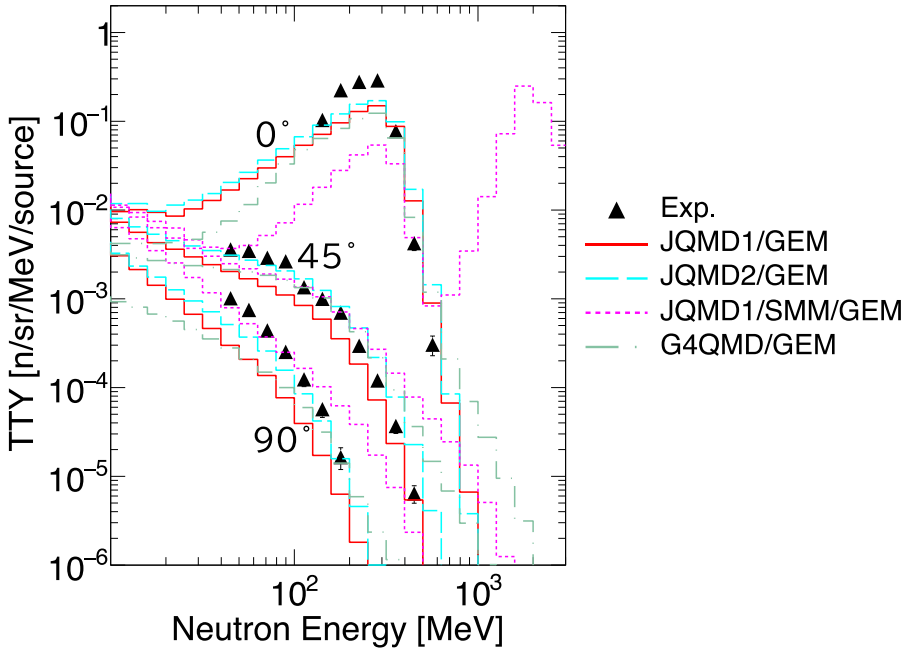

Focusing on Quasi-Free Scattering (QFS) region at 0˚, all of the models underestimate the measured data. Especially, this tendency is remarkable for JQMD1/SMM/GEM. The best agreement at QFS region is observed between the measured data and JQMD2/GEM. Above the QFS region, most of the calculations overestimate the measured data. For the JQMD1/SMM/GEM, a peak around 2 GeV is appeared. Because this peak might cause the overestimation extremely for neutron dose rate, we concluded that JQMD1/SMM/GEM is not preferable for estimating the neutron source term at 0˚ for the reaction of interest.

At energy region below 100 MeV for 45˚, all models underestimate the measured data. In this energy range, the best agreement between the measured data and JQDM2/GEM is confirmed. On the other hand, the tendency of the overestimation above 100 MeV is observed except for JQMD1/GEM. As the similar trend seen at 0˚, higher-energy neutrons are generated with JQMD1/SMM/GEM.

At energy region below 100 MeV for 90˚, all models underestimate the measured data. Particularly, JQMD1/GEM and G4QMD/GEM has the remarkable trend. Best agreement between the measured data and JQMD1/SMM/GEM is demonstrated in this energy range. The tendency of the underestimation is kept at the energy region above 100 MeV for 90˚ except for JQMD1/SMM/GEM.

For the total neutron yields, the TTY at QFS region is dominant. Thus, we conclude that JQMD2/GEM is the most appropriate to estimate the total neutron yields.

1.4. Summary and Conclusions

According to the measured data of the neutron production TTYs from 345 MeV/u ^{238}U incidence on Cu, the benchmark study of nuclear reaction models was carried out in this

study. We compared the measured data with JQMD1/GEM, JQMD2/GEM, JQMD1/GEM/SMM, and G4QMD/GEM to understand which nuclear reaction model is the most suitable for estimating the neutron source term. Our conclusion is that JQMD2/GEM is the best to estimate the total neutron yields for the reaction in question.

1.5. References

Fujiki K. *et al.* (2019), "^{211}At-labeled immunoconjugate via a one-pot three-component double click strategy: practical access to α-emission cancer radiotherapeutics", Chem. Sci. 10, pp. 1936-1944.

Ahn D.S. *et al.* (2019), "Location of the neutron dripline at fluorine and neon", Phys. Rev. Lett. 123, 212501.

Suzuki H. *et al.* (2013), "Production cross section measurements of radioactive isotopes by bigrips separator at RIKEN RI beam factory", Nucl. Instrum. Methods B 317, pp. 323-332.

Wei J. *et al.* (2019), "Advances of the FRIB project", Internat. J. Modern Phys. E 28, 1930003.

Augostin I. *et al.* (2018), "Status of the FAIR Project", in: Proc. 9th International Particle Accelerator Conference, pp. 63-68.

Kim Y.J. *et al.* (2020), "Current status of experimental facilities at RAON", Nucl. Instrum. Methods B 463, pp. 408-414.

Yano Y. *et al.* (2007), "The RIKEN RI beam factory project: A status report", Nucl. Instrum. Methods B 261, pp. 1009-1013.

Uwamino Y. *et al.* (2000), "Shielding design of RIKEN RI beam factory", J. Nucl. Sci. Technol. 37 (sup1), pp. 146-149.

Moyer B.J. (1962), "Method of calculation of the shielding enclosure for the berkeley bevatron", in: Proc. 1st Int. Conf. Shielding Around High Energy Accelerators, Vol. 65, Presses Universitaires de France, Paris.

Kurosawa T. *et al.* (2000), "Measurements of thick target neutron yields from 100 to 800 MeV/nucleon heavy ions", J. Nucl. Sci. Technol. 37 (sup1), pp. 135-141.

Niita K. *et al.* (1995), "Analysis of the (n, xn') reactions by quantum molecular dynamics plys statistical decay model", Phys. Rev. C 52 (2620), pp. 2620-2635.

Ogawa T. *et al.* (2015), "Energy dependent fragmentation cross sections of relativistic ^{12}C", Phys. Rev. C 92, 024614.

Furihata S. (2000), "Statistical analysis of light fragment production from medium energy proton-induced reactions", Nucl. Instrum. Methods B 171, pp. 251-258.

Sato T. *et al.* (2018), "Features of particle and heavy ion transport code system (PHITS) version 3.02", J. Nucl. Sci. Technol. 55, pp. 684-690.

Ogawa T. *et al.* (2013), "Analysis of multi-fragmentation reactions induced by relativistic heavy ions using the statistical multi-fragmentation model", Nucl. Instrum. Methods A 723, pp. 36-46.

Tatsumi K. (2010), "New native QMD code in Geant4", in: Joint International Conference on Supercomputing in Nuclear Applications and Monte Carlo 2010 (SNA+MC2010).

Allison J. *et al.* (2016), "Recent developments in geant4", Nucl. Instrum. Methods A 835, pp. 186-225.

Sugihara K. *et al.* (2022), “Measurement of neutron energy spectra of 345 MeV/u ^{238}U incidence on a copper target”, Nucl. Instrum. Methods B 512, pp. 102-107.

2. Photo-neutron emission mechanism at low-energy photon interaction

Mahdi Bakhtiari [1], Nam-Suk Jung [2], Hee-Seock Lee[1,2*]
[1]Division of Advanced Nuclear Engineering, POSTECH, Pohang 37673, Republic of Korea
[2]Pohang Accelerator Laboratory, POSTECH, Pohang 37673, Republic of Korea
[*]lee@postech.ac.kr

A photonuclear reaction consists of the photoabsorption and particle emission. Once the photon is absorbed, the excited nucleus decays via direct, preequilibrium and compound (evaporation) mechanisms. Photoneutron production yields and production mechanisms were investigated by comparing results of the well-known estimation methods. Differential photoneutron yields from ^{nat}Pb,^{197}Au, ^{nat}Sn and ^{nat}Cu targets irradiated with 16.6 MeV photons were calculated using PHITS-3.1, FLUKA 4-2.1, and MCNP6.1. The results were compared with the experimental data in the literature. Compound, preequilibrium and direct reaction contributions to neutron double differential cross sections were calculated by TALYS. All Monte Carlo codes generated the compound part of neutron spectra well but failed at higher energy range. MCNP6.1 using ENDF/B-VII.0 and IAEA/PD-2019 libraries showed more reasonable data than PHITS and FLUKA. MCNP6.1 with ENDF/B-VII.0 reproduced the neutron spectra up to 8 MeV for ^{197}Au target and agreed well with the experimental data. Results in this study showed the necessity of improvement of nuclear data libraries or nuclear models implemented in the codes for describing photonuclear reactions beyond the evaporation (compound) part which are namely preequilibrium and direct mechanisms. The full data in this study are found in reference paper (Bakhtiari, Jung and Lee, 2022).

2.1. Introduction

Photons with energies above a few MeV can generate photoneutrons after interacting with materials. The produced photoneutrons are of importance in radiological concerns in radiation protection. In addition, it can be utilized as neutron sources for different applications such as Bragg edge imaging (H. Sato *et al.*, 2018; Kino *et al.*, 2019).
A photonuclear reaction is assumed to be consisted of photoabsorption process and particle emission. The absorption of incident photon by the target is governed by giant-dipole resonance (GDR) and quasi-deuteron (QD) mechanisms. For photon energies lower than 30 MeV, the photoabsorption is determined by GDR and up to around 150 MeV, it is described by QD (Chadwick *et al.*, 2003). On the other hand, the target nucleus which is excited by the absorbed photon, decays via direct, preequilibrium and compound mechanisms. In the direct reactions, the residual nucleus is left in the ground or first excited states so that the emitted neutrons form the high energy part of the spectrum. The preequilibrium mechanism becomes important at incident photon energies above 10 MeV (Chadwick and Young, 1995). The emitted particles resulted from the preequilibrium mechanism forms the emission spectra between the compound and the direct mechanisms. There are numerous measured neutron angular distributions in the literature that have been performed using the bremsstrahlung beams rather the monoenergetic photons. Recently, the laser Compton backscattering (LCS) technique has made it possible to produce polarized quasi monenergy photons (Asano, Miyamoto and LEPS-II collaboration, 2014). Two sets of measured data by Kirihara et al. (2019) and Tuyet et al. (2021) were conducted using the LCS polarized photons with energy of 16.6 MeV on different targets and they measured the photoneutron production yields at different angles. However, there was a lack of comparison of the measured photoneutron yields with the Monte Carlo calculations. Therefore, the Monte Carlo calculations were performed in this work and were compared

with the experimental data by Kirihara et al. and Tuyet et al. Moreover, the contribution of each reaction mechanism to the photoneutron production yields were investigated. Here, the neutron production yields from ^{197}Au(γ,xn) reaction calculated by the Monte Carlo codes are compared with the experimental data (Kim Tuyet *et al.*, 2021).

2.2. Methods

The Monte Carlo codes PHITS-3.1 (T. Sato *et al.*, 2018), FLUKA 4-2.1 (Battistoni *et al.*, 2015) and MCNP6.1 (Goorley *et al.*, 2013) were used to calculate the neutron production yields for the 16.6 MeV photon-induced reactions. The experimental data performed by Tuyet et al. were obtained using the polarized photons. Two photonuclear cross section libraries, ENDF/B-VII.0 (Chadwick *et al.*, 2006) and IAEA/PD-2019 (Kawano *et al.*, 2020) as well as physics models were used in the MCNP6.1 code. In case of using the physics model in MCNP, the Lorentzian function is used at the giant dipole region (GDR) for calculating the photonuclear cross sections. The total photonuclear cross sections are evaluated in JENDL/PD-2004 (Kishida *et al.*, 2005) library and are used in the PHITS code. The neutron production from excited nucleus is estimated by Generalized Evaporation Model (GEM) (Furihata, 2000). The FLUKA code uses the IAEA photonuclear cross section library as well as other experimental data (Fassò, Ferrari and Sala, 2005) and cannot be manipulated by the user. In a case that the library does not have the photonuclear cross sections, they are calculated based on the Lorentzian function at the GDR region. After the photon is absorbed by the nucleus, nuclear effects on the initial and final state such as reinteraction or emission of reaction products are considered in FLUKA hadronic interaction model PreEquilibrium Approach to NUclear Thermalization (PEANUT) (Battistoni *et al.*, 2015).

In this simulation, a cylindrical target with thickness and diameter of 1 cm was irradiated with 16.6-MeV monoenergy photons. The differential photoneutron yields from ^{nat}Pb,^{197}Au, ^{nat}Sn and ^{nat}Cu targets were calculated by means of the Monte Carlo codes (Bakhtiari, Jung and Lee, 2022). The results were calculated at 30°, 60°, 90°, 120° and 150°, which are the angles between detectors and photon beam. In the Monte Carlo codes, the polarized photons cannot be defined so as the photon beam is unpolarized. The calculated results were compared with the experimental data (Kim Tuyet *et al.*, 2021) and the results of 30° are only shown here. The comparison of the calculated neutron yields at different angles and for other materials are discussed and compared with the measured data in our previous work (Bakhtiari, Jung and Lee, 2022). In this paper, only the comparison results of a cylindrical ^{197}Au target is introduced. TALYS-1.95 (Koning, Hilaire and Goriely, 2019) was also used to calculate the double differential cross sections (DDX) of ^{197}Au(γ,xn) reaction to investigate the contributions of each mechanism to the neutron production yields.

2.3. Results

The double differential cross sections of ^{197}Au(γ,xn) reaction were calculated using TALYS-1.95 to illustrate the contributions of abovementioned mechanisms to the neutron emission spectrum, and the results are shown for comparison in Figure 2.1. These results indicate that the compound mechanism is dominant up to the emitted neutron energy of 4 MeV for this reaction. After that the preequilibrium becomes important in the neutron emission process. The direct contribution is very small. The data by Tuyet et al. were measured using polarized photons with the polarization angle of 0° and are shown in Figure 2.2. It is seen that all the codes regenerate the compound (evaporation) part of the spectrum well. Generally, MCNP6.1(ENDF/B-VII.0) is more consistent with the experimental data up to 8 MeV. The PHITS data drop at the emitted neutron energy of

4 MeV because it does not consider the preequilibrium mechanism at this incident photon energy. FLUKA, MCNP6.1(IAEA/PD-2019) and MCNP6.1(physics-Lorentzian) results tend to be larger than PHITS results as they consider preequilibrium mechanism into account. However, they still underestimate the experimental data. All the codes failed to reproduce the experimental data above emitted neutron energy of 8 MeV which are related to the direct mechanism. These results show that the compound mechanism is dominant up to emitted neutron energy of 4 MeV for photonuclear reaction. Above this energy, the preequilibrium mechanism becomes important in the neutron emission process. The models that describe the direct mechanism are insufficient in the Monte Carlo codes. Therefore, the direct mechanism contribution to the calculated neutron production yields is negligible so that the Monte Carlo codes underestimate the experimental data at high emitted neutron energies.

Figure 2.1. Contribution of compound, preequilibrium and direct mechanisms to the DDX calculated by TALYS.

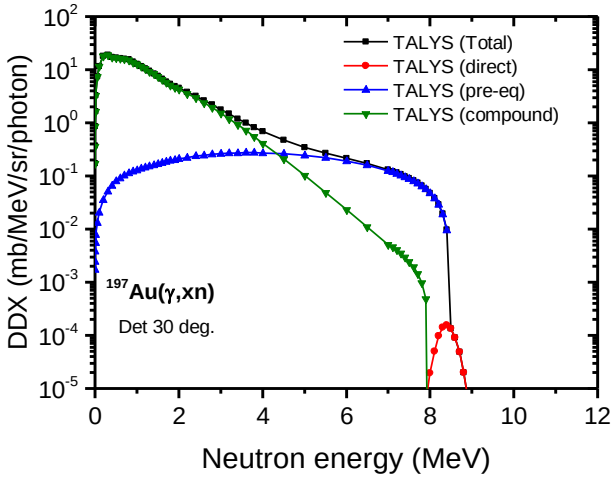

Figure 2.2. Experimental and calculated photoneutron production yields at 30° from ^{197}Au target induced by 16.6-MeV photons.

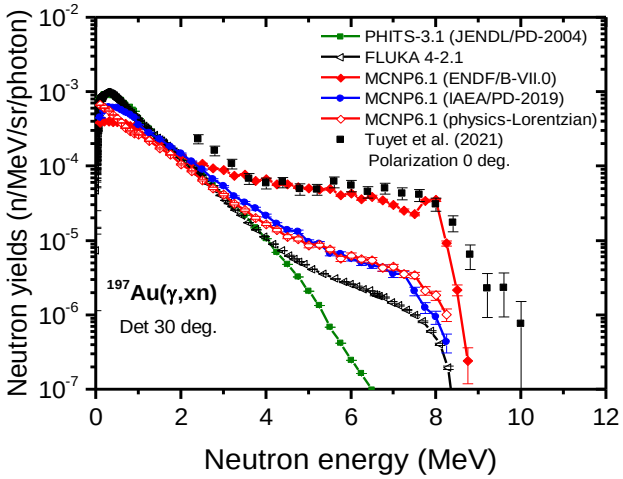

2.4. Summary and Conclusions

The contributions of the compound, preequilibrium and direct mechanisms to the photoneutron emission were investigated for 16.6 MeV photon induced reactions. Three Monte Carlo codes as well as TALYS-1.95 were used in this work. The preequilibrium mechanism becomes important above the emitted neutron energy of 4 MeV for ^{197}Au(γ,xn) reaction. MCNP6.1(ENDF/B-VII.0) could reproduce the experimental data well up to 8 MeV. All the codes could not reproduce the high energy neutrons. The monoenergetic photons play a very important role to study the photonuclear reactions and its governing physics. It is concluded that the nuclear data libraries and nuclear models describing photonuclear reactions in the Monte Carlo codes need to be improved especially above the evaporation part.

2.5. List of references

Asano, Y., Miyamoto, S. and LEPS-II collaboration (2014) "Shielding design of laser electron photon beamlines at SPring-8", Progress in Nuclear Science and Technology, 4(3), pp. 252–256. DOI: 10.15669/pnst.4.252.

Bakhtiari, M., Jung, N. S. and Lee, H. S. (2022) "Contribution of compound, preequilibrium and direct reactions to photoneutron emission spectrum from various targets induced by 16.6-MeV monoenergetic photons", Nuclear Instruments and Methods in Physics Research, B 521(2021), pp. 38–46. DOI: 10.1016/j.nimb.2022.03.007.

Battistoni, G. et al. (2015) "Overview of the FLUKA code", Annals of Nuclear Energy, 82, pp. 10–18. DOI: 10.1016/J.ANUCENE.2014.11.007.

Chadwick, M. B. et al. (2003) "Photonuclear physics in radiation transport—I: Cross sections and spectra", Nuclear Science and Engineering, 144(2), pp. 157–173. DOI: 10.13182/NSE144-157.

Chadwick, M. B. et al. (2006) "ENDF/B-VII.0: Next generation evaluated nuclear data library for nuclear science and technology", Nuclear Data Sheets, 107(12), pp. 2931–3060. DOI: https://doi.org/10.1016/j.nds.2006.11.001.

Chadwick, M. B. and Young, P. G. (1995) "Preequilibrium model for photonuclear reactions up to the pion threshold", Acta Physica Slovaca, 45, pp. 633–644.

Fassò, A., Ferrari, A. and Sala, P. R. (2005) "Photonuclear reactions in FLUKA: Cross sections and interaction models", AIP Conference Proceedings, 769(1), p. 1303. DOI: 10.1063/1.1945245.

Furihata, S. (2000) "Statistical analysis of light fragment production from medium energy proton-induced reactions", Nuclear Instruments and Methods in Physics Research, Section B 171(3), pp. 251–258. DOI: 10.1016/S0168-583X(00)00332-3.

Goorley, J. T. et al. (2013) Initial MCNP6 release overview-MCNP6 version 1.0.

Kawano, T. et al. (2020) "IAEA photonuclear data library 2019", Nuclear Data Sheets, 163, pp. 109–162. DOI: 10.1016/J.NDS.2019.12.002.

Kim Tuyet, T. et al. (2021) "Energy and angular distribution of photo-neutrons for 16.6 MeV polarized photon on medium–heavy targets", Nuclear Instruments and Methods in Physics Research, A 989, p. 164965. DOI: 10.1016/J.NIMA.2020.164965.

Kino, K. et al. (2019) "Design of a compact electron accelerator-driven pulsed neutron facility at AIST', Nuclear Instruments and Methods in Physics Research, A, 927, pp. 407–418. DOI: 10.1016/j.nima.2019.02.062.

Kirihara, Y. et al. (2019) “Neutron emission spectrum from gold excited with 16.6 MeV linearly polarized monoenergetic photons”, Journal of Nuclear Science and Technology, 57(4), pp. 444–456. DOI: 10.1080/00223131.2019.1691073.

Kishida, N. et al. (2005) “JENDL photonuclear data file”, AIP Conference Proceedings, 769, pp. 199–202. DOI: 10.1063/1.1944989.

Koning, A. J., Hilaire, S. and Goriely, S. (2019) “User manual of TALYS-1.95”, http://www.talys.eu/download-talys.

Sato, H. et al. (2018) “High wavelength-resolution Bragg-edge/dip transmission imaging instrument with a supermirror guide-tube coupled to a decoupled thermal-neutron moderator at Hokkaido University Neutron Source”, Physica B: Condensed Matter, 551, pp. 452–459. DOI: 10.1016/j.physb.2017.12.058.

Sato, T. et al. (2018) ‘Features of particle and heavy ion transport code system (PHITS) version 3.02’, Journal of Nuclear Science and Technology, 55, pp. 684–690. DOI: 10.1080/00223131.2017.1419890

2.6. List of abbreviations and acronyms

GDR	Giant dipole resonance
QD	Quasi deuteron
LCS	Laser Compton backscattering
ENDF	Evaluated nuclear data file
IAEA	International atomic energy agency
JENDL	Japanese evaluated nuclear data file
PD	Photonuclear data
PEANUT	PreEquilibrium Approach to NUclear Thermalization
DDX	Double differential cross section

3. Impact of new delivery methods in proton therapy on radiation protection of Compact Proton Therapy Centers (CPTC)

Gonzalo F. García-Fernández[1*], Eduardo Gallego[1], José M. Gómez-Ros[2], Alejandro Carabe-Fernández[3], Alejandro Bertolet-Reina[4]

[1]Department of Energy Engineering, Nuclear Area, Universidad Politécnica de Madrid, Madrid, Spain
[2]CIEMAT, Madrid, Spain
[3]HUPTI, Hampton University Proton Therapy Institute, Virginia, USA
[4]MGH, Massachusetts General Hospital, Boston, Massachusetts, USA

[*]gf.garcia@upm.es

In their eagerness to improve clinical results, the delivery methods in proton therapy are moving towards more precise techniques with the goal of increasing their therapeutic index (TI). Once the primal passive scattering methods were overcome by current active scanning process, the evolution continues and new methods such as arc therapy, proton minibeams or flash therapy, among others, are currently in several stages of development and research. For example, Proton Monoenergetic Arc Therapy (PMAT) uses isoenergetic fields from 360º degrees, with lower energies than conventional ones, but for a longer time. On the other hand, Proton Flash-Therapy (PFT), usually involves dose rates above 40 Gy/s, much bigger than around 0.1 Gy/s in current treatments, which supposes pulsed neutron fields of high energy and intensity. Obviously, trials of these methods are carried out in existing facilities, so the big question would be if the radiation protection measures in current proton centers are ready for the fresh challenges. Consequently, the main goal of this work has been to develop comparative analysis, using Monte Carlo codes (MCNP and PHITS) and experimental measurements, of the impact on the radiation protection of different proton dose delivery modes under development. The new delivery methods compared were PMAT and PFT against the current Intensity Modulated Proton Therapy (IMPT). For PMAT, both experimental measurements and simulations with MCNP6 and PHITS codes have been reached. For PFT, only calculation with Monte Carlo methods has been developed. Results show that with PMAT, higher neutron fluences are generated, but with lower energy, therefore, its impact is greater on activation, but lower on the ambient dose equivalent, hence, the shielding requirements could be reduced. However, for PFT mode, current shielding should be reviewed with caution since the energies used are the higher and the Instantaneous Doses Rates (IDR) outside walls could overtake legal limits in some cases, depending on the country. Mitigating actions could be limiting orientation of beam and occupancies in some spaces, using special concretes in different areas, or change the design and location of treatment control room. Experimental measurements could help to achieve more precise assumptions, but neutron monitors must be able of measuring high-energy neutrons in pulsed fields. Active measurements should be supported with reliable data from passive monitors. Evenly, the impact over others relevant aspect of radioprotection, as activation or personal dosimetry should be carefully reviewed.

3.1. Introduction

Radiotherapy is a discipline in continuous evolution, with increasing speed of change, as well as particle therapy in general, and particularly proton therapy. Over the years, clinical radiotherapy treatments have undergone different improvements to achieve their main goal,

which is to kill cancer cells through enough irradiation of tumoral tissues, while protecting surrounding healthy structures, as much as possible (Carabe *et al*., 2020a).

This could be assessed by the so-called *Therapeutic Index* (*TI*), which relates *Tumour Control Probability (TCP*), and *Probability of Normal Tissue Complication* (*NTCP*). Improvements in delivery methods seek to increase *TI*, however, there is always a trade-off in increasing the amount of dose delivered to the tumour, as normal tissue is simultaneously exposed to damaging radiation (Paganetti *et al.*, 2021).

A key aspect with radiation treatments is the method use to deliver the dose, since generation of secondary radiation is highly dependent on the elements used in the line and *nozzle* to shape the tumour. In proton therapy and charged particles radiotherapies, the target volume is covered by the transverse and longitudinal *Spread-Out Bragg Peaks* (*SOBP*). With passive systems, this is accomplished by combining some metallic and plastics elements as scatterers, range shifter, collimator and *SOBP* modulator, with the result of generating a large amount of secondary radiation, and unnecessary exposure to normal tissues. With active methods, using *Pencil Beam Scanning* (*PBS*), the target coverage is achieved by scanning the beam laterally, in *x and y axis*, respectively, and delivering spots at a given depth, in consecutive layers of different energy, from the *distal* to the *proximal*, until the irradiation of the whole volume. The cornerstone of current active methods is *IMPT*, *Intensity Modulated Proton Therapy* (Alshaikhi *et al*., 2021).

New delivery modes are under investigation, such as *Proton Flash Therapy* (*PFT*), an emerging technique with significant interest and a great potential to revolutionize radiotherapy, by targeting an increase in the *TI* due to the biologic advantages of reduced normal tissue complications through the tissue-sparing *flash effect*. Although there is no general criterion at the moment, *PFT* involves dose rates above *40 Gy/s*, much bigger than around *0.1 Gy/s* in current treatments. Other methods under study are *Proton Monoenergetic Arc Therapy* (*PMAT*), and *Proton Minibeams* (*PMB*). In any case, changes and developments in technical systems and equipment of proton therapy facilities always have an impact on the generation of secondary radiation, sometimes reducing it, and others just the opposite, elsewhere, it should be necessary to develop a suitable methodology to assess the impact of new delivery methods on radiation protection (Mazal *et al.*, 2021).

Consequently, the goal of this work was to carry out a comparative analysis between the secondary neutron fields produced with some of new delivery modes currently under development, *PMAT* and *PFT*, compared with *IMPT*, the current standard scanning method used in most proton therapy centers around the world.

In the *benchmark* of *PMAT* versus *IMPT*, both, experimental measurements, and simulations with *PHITS Monte Carlo* code, were carried out. Measurements were reached at different distances and angles from the cylindrical *phantom* used in radiobiological tests. To achieve an approximate but real continuous *arc irradiation*, the proton beam was delivered following a constant direction, while the *phantom* rotates with a predetermined speed to reach the planned dose distribution over the different cell colonies on *Petri plates*, placed inside the *phantom*. These experimental data were developed in the *Fixed Beam Treatment Room* (*FBTR*) of the *Roberts Proton Therapy Center* (*RPTC*), at the University of Pennsylvania (*UPenn)*, at the same time as the comparative studies on radiobiological effectiveness with both treatments, developed by Professor Carabe-Fernández and his team over the last few years (Carabe *et al*., 2020b), (Bertolet and Carabe, 2020). Experimental measurements were carried out using *PRESCILA* (*Proton Recoil Scintillator-Los Alamos*), a scintillator neutron detector with a range of *several hundred of MeV* (Olsher *et al.*, 2004).

In the *benchmark* of *PFT* versus *IMPT*, exclusively simulations with *PHITS*, *Monte Carlo* codes were developed.

3.2. Benchmarking of neutron dose equivalent of *PMAT* versus *IMPT*

a. Characterization and goals in radiobiological experiments with *PMAT*

Specific details and complete features of radiobiological experiments are collected elsewhere, (Carabe *et al.*, 2020b), and (Bertolet and Carabe, 2020). All data of treatments in this section are selected from such references. Radiobiological experiments employed a cylindrical rotating *phantom*, similar as shown in Figure 1.1.

Figure 3.1 Details of cylindrical phantom and dosimetric characteristics with *IMPT* and *PMAT*

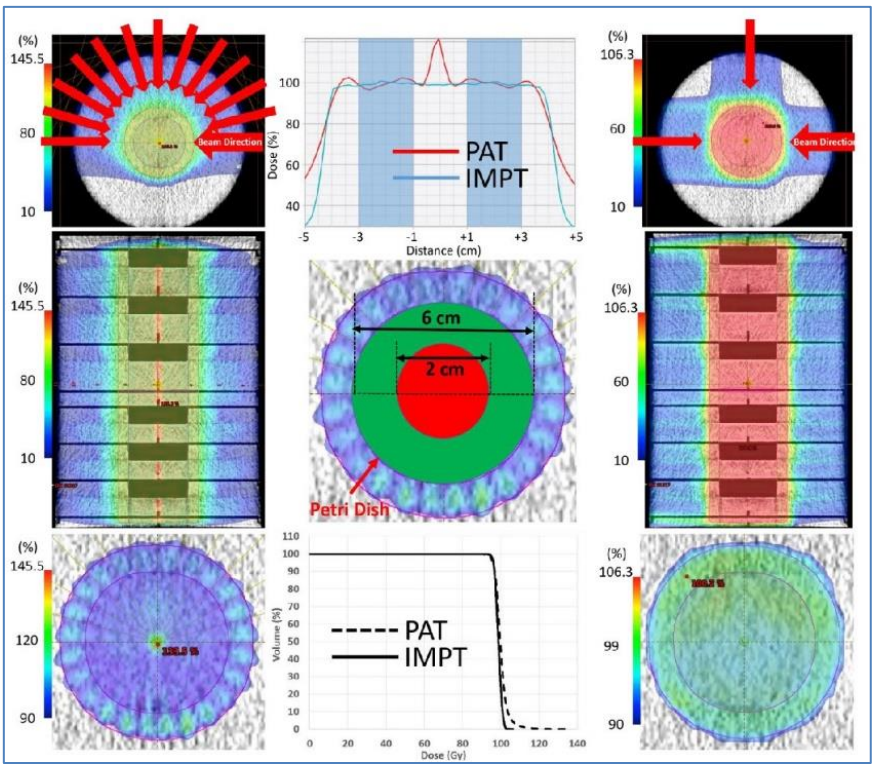

Source Carabe et al. (2020b)

The cylindrical *phantom* has several hollows to place *Petri dishes* with different types of cells inside, checking the damage by irradiation with proton delivery modes under study. The proton beam has a fixed direction, while the *phantom* rotates with a predetermined speed, depending on the final dose planned, reaching at this way the irradiation type in *arc*.

Simultaneously with radiobiological experiments, ambient dose equivalent by neutrons, *H*(10)*, was measured, at different distances and angles from the cylindrical *phantom*.

b. Equivalent dosimetric plans

Complete irradiation plans and full dosimetric details with both modalities, *IMPT* and *PMAT*, are equivalent, with a planned clinical dose of *6 Gy*. Each *PMAT* treatment is dose-equivalent to *IMPT* treatment with three fields at *90°*, as collected in Figure 3.1.

To develop experimental measurements of neutron doses, a number of *36 irradiations* were carried out, *19* with *PMAT* and *17* with *IMPT*, respectively The mean (absolute) clinical dose delivered with *PMAT* was *14,090 Monitor Units* (*MU*), with a mean irradiation time of *7 minutes*, *44 seconds* (*464 seconds*) per treatment, and a constant range of *10.1 g/cm*^{2}, that means the radius of the cylindrical *phantom*, and a energy of *117.15 MeV*.

On the other hand, with *IMPT*, the mean (absolute) clinical dose delivered per field was *3,840 MU*, with a mean irradiation time of *1 minute, 11 seconds* (*71 seconds*), and a maximum range of *14.12 g/cm²*, corresponding to the maximum energy of *141.7 MeV*, with a modulation in *13 layers*, up to *6.31 g/cm²*, which represents an energy of *89.5 MeV*.

The range of energies with *PMAT* roughly covers the outer layer of the *phantom* (*6.15 cm*), plus the diameter of the hollow for *Petri dishes* (*7.7 cm in total*). The ionization chamber calibration for absolute dosimetry was *3 nC per MU*, and the air gap, *d=0.2 cm*. *MU* is the system used in many centers to control and verify the dose delivered in the treatments

c. Experimental configuration and set-up

The three main elements of the experimental configuration considered in the work were the *Fixed Beam* (*FBTR*), the rotating cylindrical *phantom*, and the *PRESCILA* device.

Geometric and technical features of cylindrical *phantom* (*diameter 20 cm*), as well as composition and other elements, are equally included in the works mentioned, (Carabe-Fernández *et al.*, 2020b), and (Bertolet and Carabe, 2020), respectively.

Figure 3.2 Experimental setup in the *Fixed Beam Treatment Room* (*FBTR*) of *RPTC* (UPenn)

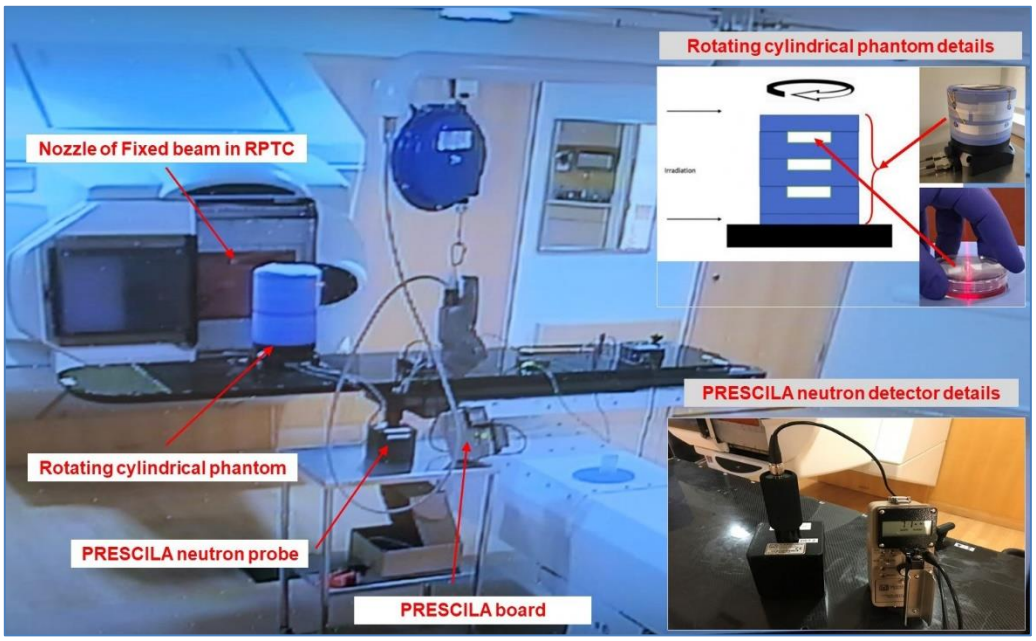

The Figure 3.2 shows the nozzle of the fixed beam (*FBTR*), the rotating *phantom* (in *dark blue*) on top of the couch, as well as the *PRESCILA* detector, in middle of the picture.

Upper right of the figure, several details of cylindrical *phantom* are collected, including hollows for *Petri dishes*, and the swivel base (in *black*).

d. Operational quantity and points of measurements neutron fields

The operational quantity for benchmarking was the ambient dose equivalent, *H*(10)*. The points around the center of *phantom*, where experimental measurements were carried out, both with *PMAT* and *IMPT* modes, are shown in next Figure 3.3. *Positions 1 to 5* are placed at *1m* from the center of the cylindrical *phantom*, whereas *Positions 1' to 5'*, are placed at *1.8 m*. The angles of measurements are between *-90º to 90º*, at intervals of *45º*, considering the irradiation direction of the proton beam in the picture (*FBTR*) as *0º*. Thus, the total number of positions were *10 points*, marked with a *green dot* in the Figure 3.3.

Figure 3.3 Location of the measurement points with respect to the *isocenter*

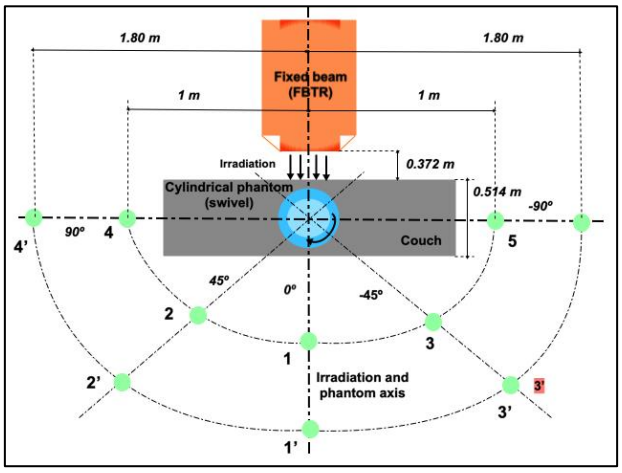

The *isocenter* is the crossing point between the axis of irradiation and the axis of the couch, at the vertical midpoint of the cylindrical *phantom*.

e. *PRECILA* neutron detector

The neutron detector, *PRESCILA*, is an scintillator type, and can work in a range up to hundreds of MeV. The characterization of the device was carried out considering a calibration factor, *C=420 pSv/count*, according to data (Olsher *et al.*, 2004).

f. Results reached comparing *PMAT* versus *IMPT*

Figure 3.4. shows values of *H*(10)* for both modes of protons delivery, *IMPT* and *PMAT*, respectively, at *1 m* (*Positions 1 to 5*), and *1.8 m* (*Positions 1' to 5'*), from *isocenter*. In *IMPT*, only a single irradiation field was considered, corresponding to *3,840 MU*. Uncertainties assumed in positions and measurements were *below 10%*.

Figure 3.4 Comparation of *H*(10) IMPT/PMAT* at *1 m* and *1.8 m*, *IMPT* with one field

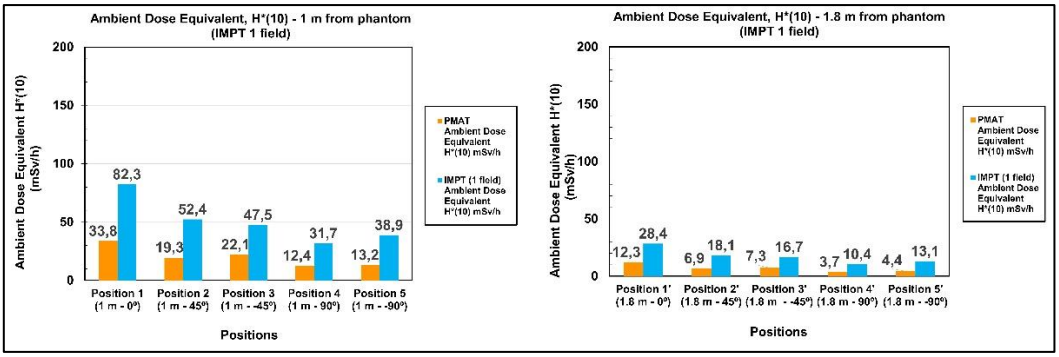

As observed in Figure 3.4, the neutron dose with both, *PMAT* and *IMPT* (with a single fied) has the same order of magnitude. The greater the distance from *phantom*, the more similar the ambient dose with both delivery modes, however, the dose with *IMPT* is almost three times that with *PMAT*. Higher neutron generation is in *Position 1*, opposite to irradiation direction (*0º*), with neutrons from spallation reactions and evaporation processes.

On te other hand, next Figure 3.5 shows values of *H*(10)*, with the same assumptions as in Figure 3.4, but now considering three fields of irradiations for *IMPT*, with an absolute dose per field of *3,840 MU*. The angle between the three fields was *90º*, as shown in Figure 3.1.

Figure 3.5 Comparation of *H*(10) IMPT/PMAT* at *1 m* and *1.8 m*, *IMPT* with three fields

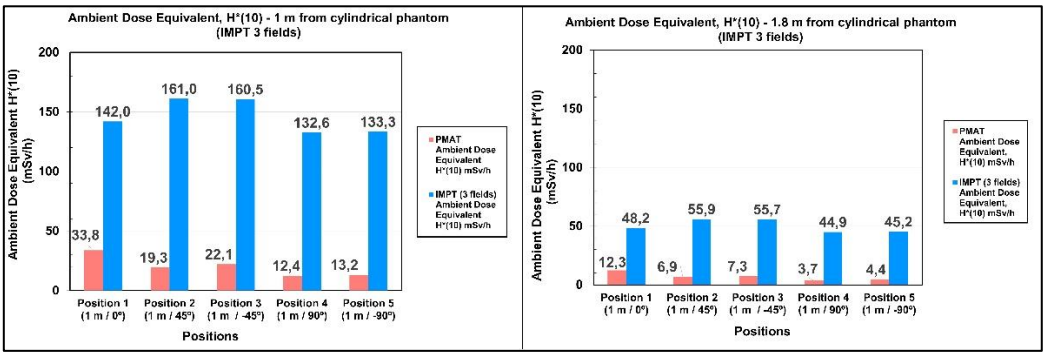

As observed in Figure 3.5, the dose with *PMAT* is logically the same, because irradiation plans are the equals, however, the dose with *IMPT*, considering now three irradiation fields, is *from 5 to 10 times higher* than dose with *PMAT*, depending on the position. In Figure 3.4 and 1.5, ambient doses are not totally symmetrical, because the room is not symmetrical either, and the neutron backscaterring is slightly different.

Neutron detector *PRESCILA*, directly measures ambient dose equivalent, *H*(10)*, using its calibration factor, therefore, to roughly estimate neutron yielding in each treatment mode, a model of the *Fixed Beam Treatment Room* (*FBTR*) was developed with *Monte Carlo* code *PHITS* (Sato *et al.*, 2018), based on information from (De Smet *et al.*, 2017).

The geometry of *FBTR* is shown in Figure 3.6, with the main enclosures and materials used (conventional concrete, air, and water-equivalent phantom), and the insertion of Figure 3.3 with the locations of measurements points. The *Position 1* is in front of beam (*0º*), at *1 m* from the axis of *phantom*. The spectra at *1.8 m* from the isocenter are collected in the same figure, on the righ side, *on top* for *IMPT* (with three fields), and for *PMAT on the bottom*. The energy of neutrons yielded with *IMPT* is two orders of magnitude higher than with *PMAT*, due to the energy (range) of the protons used in the different modess, with a direct impact on both, the ambient dose and the shielding and attenuation materials in the barriers.

Figure 3.6 Comparations of experimental meassurements and calculations with *Monte Carlo*

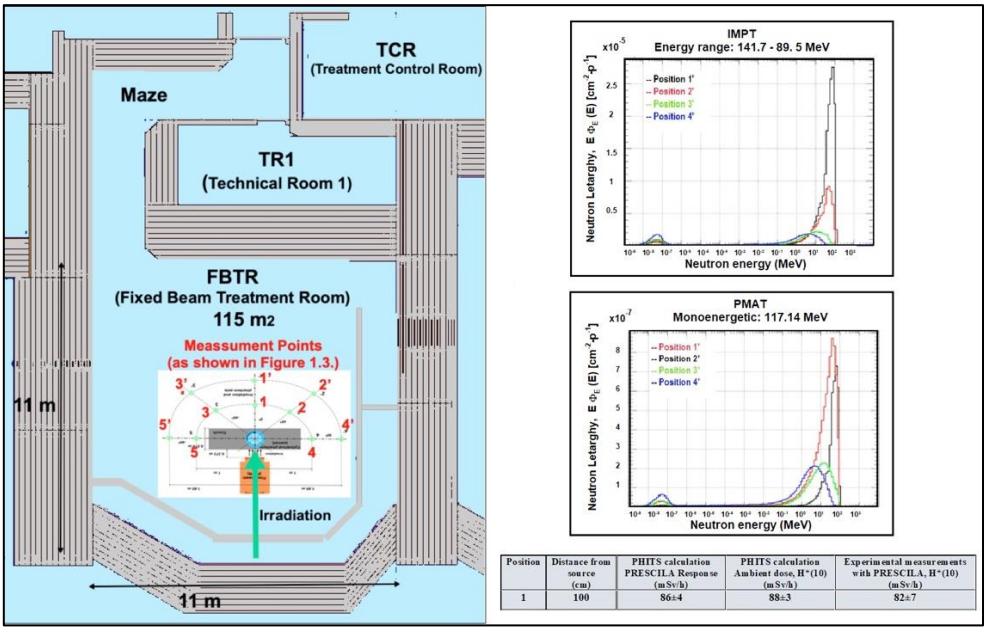

Position	Distance from source (cm)	PHITS calculation PRESCILA Response (mSv/h)	PHITS calculation Ambient dose, H*(10) (mSv/h)	Experimental measurements with PRESCILA, H*(10) (mSv/h)
1	100	86±4	88±3	82±7

Results of ambient dose equivalent *H*(10)* at *Position 1* are included in the table at the bottom of the Figure 3.6, with a value of *86 (±4) mSv/h*, when calculating the theoretical response of *PRESCILA* with *PHITS*, *88 (±3) mSv/h*, in the calculation with *PHITS*, but in this case directly *H*(10)*, and finally, *82 (±7) mSv/h*, in experimental measurements *in situ* with *PRESCILA*. Considering these results, and from the point of view of operational radiological protection, the main conclusions would be as follow:

1. For a treatment with *IMPT* with a single field, *H*(10)* has the same order of magnitude with both modes, although with *PMAT* is between two and three times lower.

2. For an equivalent treatment of *PMAT* and with *IMPT* (with three fields), *H*(10)* is *from five to ten times higher* with *IMPT* versus *PMAT*.

3. Neutrons yielding, per proton of treatment, with *IMPT* (three fields) is almost two orders of magnitude higher with *PMAT*. However, as the mean energy with *PMAT* is lower, it is necessary a higher intensity in the beam to achieve the same clinical dose (two times more).

4. The key factor of lower dose with *PMAT* is the use of lower energies in protons, monoenergetic energy of *117.14 MeV*, compared with full *SOBP* in *IMPT*, where the range varies from *141.7 MeV* for *distal* layer, *to 89.5 MeV*, for *proximal* layer.

5. The lowest generation of energetic neutrons with *PMAT* could reduce the footprint of centers, since the thickness of the shielding could be lower. However, activation of barriers could be higher with *PMAT*, because its intensity higher (Ramoisiaux *et al*., 2022).

In summary, *PMAT* would have dosimetric advantages and *LET* optimization in tumour, as shown in radiobiological works (Carabe-Fernández *et al.*, 2020b), (Bertolet and Carabe, 2020), while achieving a non-negligible reduction of secondary dose from neutrons, with a positive direct impact on both, operational radiological protection, and dose in patients.

3.3. Benchmarking of neutron dose equivalent with *PFT* and *IMPT*

a. *PFT* main features and uncertainties at the present stage of development

Ultra-high dose rate *Flash radiotherapy* has shown in several *in vivo* studies to better preserve healthy tissue with equivalent tumour control compared to traditional external beam radiotherapy at conventional dose rates. *In vitro* studies using ultra-high dose rate were also carried out to study the *Flash effect* of cell culture. The differential response in terms of normal tissue toxicity and tumour control is very attractive, as *Flash* may allow for reduced organ toxicities and/or a safer dose escalation to the tumour target than would be achievable with standard dose rates (Poirier *et al.*, 2021).

However, while preclinical results have shown significantly reduced toxicities to healthy tissues while maintaining excellent tumour control, and trials are encouraging, in the design of shielding of the current proton therapy centers, the irradiation conditions of flash therapy with protons were not considered (Xiao *et al.*, 2022). Nevertheless, in the current state of knowledge, there are several relevant uncertainties, linked to radiation protection with *PFT* irradiation mode, among which, the following could be highlighted (Zou *et al.*, 2021):

1.Currently, *PFT* involves two different methods, one by transmission, and the second known as *Bragg Peak* method, with specific features and different impact on radiation protection. The neutron fields will depend on where and how the beam is stopped in the transmission, or on how the *Bragg peak* will be shaped with *Flash*.

2. There is still no uniform criteria on dose rates for *PFT*, with figures from *10 Gy/s* to *300 Gy/s*, depending on the work consulted, however, always much bigger than *0.1 Gy/s* in current treatments. Obviously, the impact would be very different with each dose rate.

3. Currently it is unknown, and difficult to quantify in future centers, the number of treatments carried out with each modality, *IMPT*, *PMAT*, *PFT*, and others under research. Clearly, *PFT* will be a disruptive method, very tough and demanding, in terms of radiation protection conditions, with a great impact on *workload* considered in the design of center.

4. *Pulsed neutron fields* (*PNFs*) are yielded in flash treatments, hence, verifications and measurements must be carried out with suitable neutron devices, as extended-range *REM-meters* suitable for pulsed fields, supported by passive systems (without dead time). At present, only some devices could measure properly *PNFs* (Caresana *et al.*, 2022), (Zorloni *et al.*, 2022a), (Zorloni *et al.*, 2022b).

5. There are *Instantaneous Dose Rate* (*IDR*) limits in some national regulations of different countries. The critical place is the Control Room (TCR), with *Occupancy factor*, *T=1*.

Once the impact of *PFT* can be assessed because the mentioned uncertainties have been clarified, it will be certainly necessary to adapt existing facilities.

Consequently, two simple cases were simulated for this preliminary study of impact of *PFT* on Compact Centers (*CPTC*). *Case 1*, comparing *IMPT*, *PMAT* and *PFT*, with a total clinical dose of *6 Gy*, and *Case 2*, *PFT* with a dose rate of *25 Gy/s*. In both cases, the *hourly dose rate* (*HDR*) was calculated, in *uSv/h*, in the control room (*TCR*), assuming an occupancy factor, *T=1*.

b. *Case 1*: Clinical treatment with total dose of *6 Gy*, comparing three delivery modes.

The following hypothesis were assumed in each mode:

1. *IMPT*: three treatment fields at *90º*, with *SOBP*s between *141.7 MeV* and *89.5 MeV*, a modulation in *13 layers*, and irradiation time of *213 s* (dose rate, 0.028 Gy/s)

2. *PMAT*: monoenergetic beams, *117.5 MeV*, irradiation time, *464 s* (dose rate, *0.013 Gy/s*).

3. *PFT*: transmission method, beam stopping in a *40x40x40 cm^3 water phantom* placed behind the patient (cylindrical phantom), irradiation time, *0.5 s* (dose rate, *12 Gy/s*).

Code settings were the same throughout the work: a number of histories enough to achieve statistical *uncertainties under 5%*, *mix & match option*, default physics models, (*CEM03.03* for intranuclear cascade and *GEM* for evaporation), and JENDL3.3. nuclear data library.

As shown in Figure 3.7, in *Case 1*, the ambient dose rate with the three modalities would be below *10 uSv/h*. This *hourly dose rate* (*HDR*), is a practical reference for exposed workers in many countries, considering a limit of *20 mSv/year*, *and 2000-hour annual shift*. Taking *IMPT* as *baseline*, with a value of *5.1 uSv/h*, with *PMAT*, the dose rate of *2.3 uSv/h* is almost *55% lower*, while with *PFT*, the dose reached is *7.8 uSv/h*, almost *53% higher*.

Figure 3.7 *PFT*, *Case 1*, comparison of *H*(10)* with *IMPT*, *PMAT* and *PFT* for a treatment of *6 Gy*

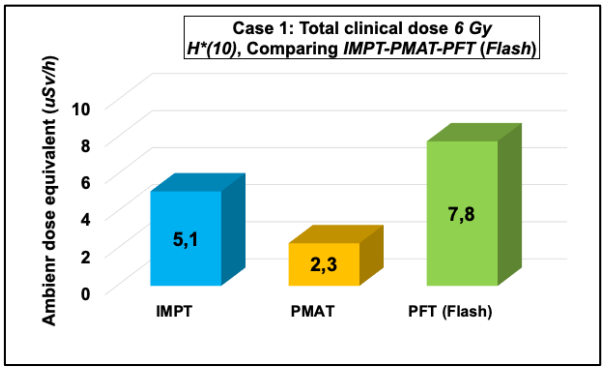

c. Case 2: Clinical treatment with dose rate of *25 Gy/s, PFT* by transmission

Assuming a tougher case of *PFT*, with a clinical dose of *12.5 Gy*, delivery time in *0,5 s*, by transmission method, and protons of *220 MeV*, dose rates of *H*(10)*, per treatment, reached at the control room (*TCR*), were *18 uSv/h*, an *80%* over the *HDR* reference of *10 uSv/h*.

Figure 3.8 *PFT, Case 2*, protons of 220 MeV, transmission mode, dose rate, *25 Gy/s*.

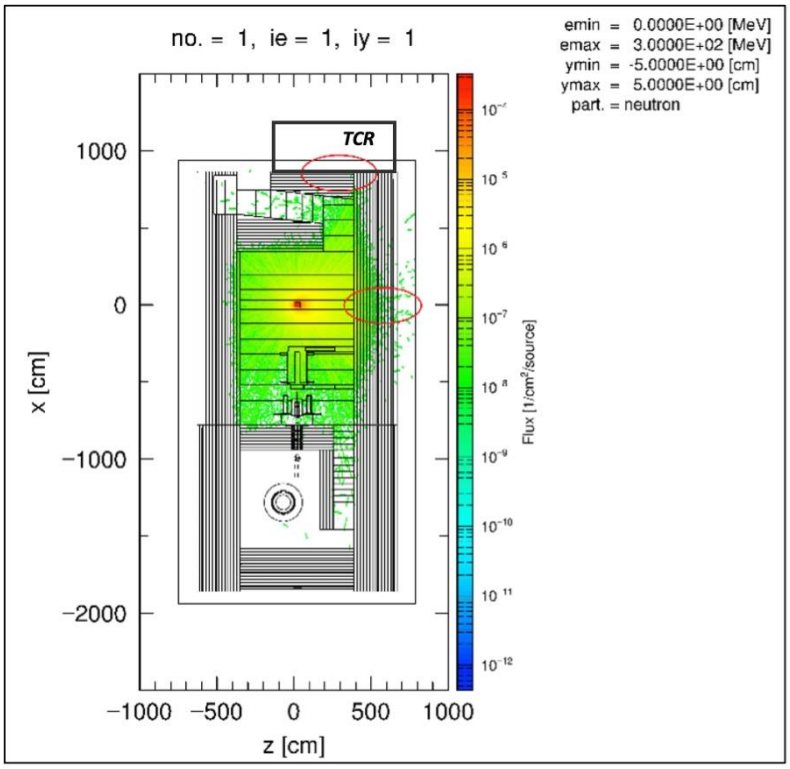

As observed in Figure 3.8 with red ellipses, the main tricky areas, from radiation protection point of view, are the corridor on the right side of the picture, just in front of the *isocenter*, and the *Treatment Control Room* (*TCR*), placed at top of the footprint.

To assess the impact of *PFT* methods, more accurately, it would be necessary to collect experimental data at the same time when the radiobiological experiments were carried on.

Some fresh papers about experimental measurements recently published conclude that current shielding is fit for *PFT* treatments (Xiao *et al.*, 2022). Measurements of the work were carried out with devices that underestimates the doses in pulsed neutron fields by *almost 40%*, so the conclusions could be a little bit hasty. Even for small pulsed fields, the performance of conventional neutron devices is not always reliable (Caresana *et al.*, 2022), (Zorloni *et al.*, 2022a), (Zorloni *et al.*, 2022b).

Therefore, it would be highly recommended to support the measurements of active devices with reliable data from passive equipment (ambient monitors, *Bonner spheres*, obviously with passive detectors), because they have no dead time, and are also insensitive to photons. The main drawback is their low sensitivity, and therefore, a long exposure time is required.

Additionally, until treatment workloads with *PFT* modality were accurately established, some short-term mitigation actions could be limiting gantry orientation to certain angles (Yan *et al.*, 2014), limiting occupancies in some spaces and areas during *PFT* irradiation, or using protective mobile screens to reduce instantaneous doses.

In the medium term, the actions could be deeper, such as changing the orientation of the control room, or using high-density concrete in the maze areas, as shown in Figure 3.9.

Figure 3.9 *PFT*, some proposal for mitigating measures in the medium term.

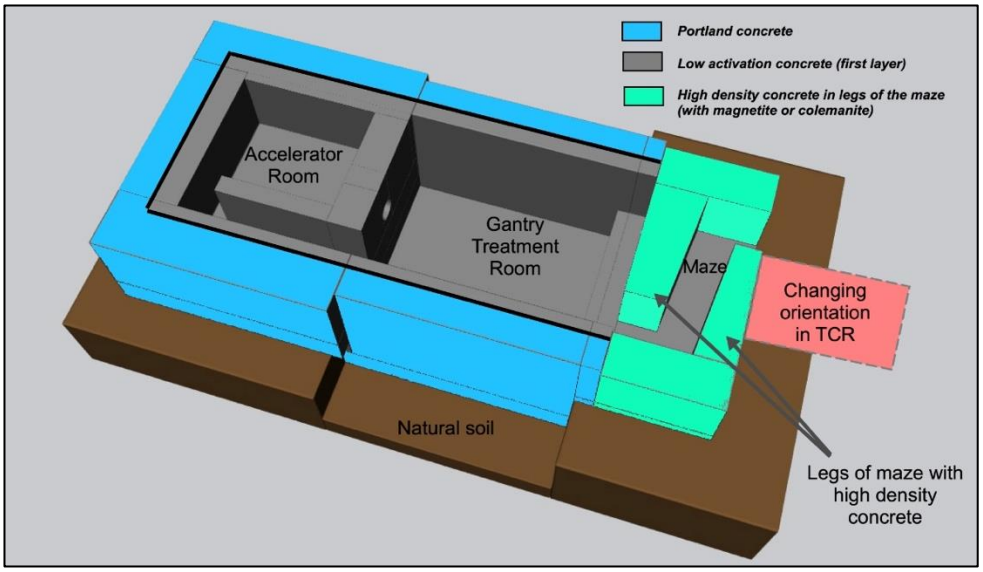

Figure 3.9 shows the area with high-density concrete (green colour), in the legs of the maze. Protection of TCR would increase, since said space would be protected by the two legs of the maze. In addition, if the orientation of *TCR* changes *90º*, this room could be protected by both legs of the maze and reducing significantly the *HDR* and consequently, yearly ambient dose. Suitable detection devices for *PNFs* of this nature, should be placed based on the expected pulse size and feature (García-Fernández *et al.*, 2023).

3.4. Summary and Conclusions

The goal of this work has been to perform a comparative analysis and benchmarking between neutron fields produced with some new proton delivery modes under development, as *PMAT* and *PFT*, and those produced with standard scanning mode currently used in most proton therapy centers around the world, *IMPT*, to assess the impact of these modalities under development, on the radiation protection of the facilities.

Results show that with *PMAT*, higher fluences of neutrons are yielded, but with lower energy, therefore, its impact is greater in activation, the higher the intensity the greater the activation, but lower in the ambient dose equivalent, hence, shielding requirements could be reduced, lowering the cost in the building of this centers.

The main reason of a lower dose with *PMAT* would be the use of proton beam with lower energies, *117.14 MeV*, compared to a full *SOBP* with *IMPT*, and energy in a range from *141.7 MeV to 89.5 MeV*. The reduction of the generation of secondary neutrons with *PMAT* could have an impact on space requirements, due to potential reduction in wall thickness of the room and reducing the footprint of centers.

In summary, *PMAT* would have dosimetric advantages and optimization of *LET* in the tumour, as collected elsewhere in corresponding radiobiological works (Carabe *et al.*, 2020b), (Bertolet and Carabe, 2020), with a non-negligible reduction of secondary neutrons, and direct positive impact, both, on operational radiation protection and on the patient.

However, for proton flash therapy, *PFT*, the advice would be the assessment of current barriers, because the energies used are the maximum, and the *IDR* outside the barriers could exceed the legal limits in some cases, depending on the country.

Mitigation actions could be limiting the gantry orientation and occupancies in some spaces, using special concretes in different areas, or changing the design and location of *TCR*.

Experimental measurements are essential and could help to do more accurate assumptions, but neutron monitors need to be able to measure high-energy *PNFs*. Active measurements must be backed up with reliable data from passive monitors. Likewise, the impact of these new dose application methods on other relevant aspects of radioprotection such as activation of air, water or ground, or personal dosimetry, should be carefully reviewed.

Acknowledgment

This work was supported by ETSII-UPM, Faculty of Industrial Engineers, Universidad Politécnica de Madrid, grant number *ETSII-UPM22-PU04*, *Primeros proyectos*.

3.5. List of references

Alshaikhi J, Doolan PJ, D'Souza D, Holloway SM, Amos RA, Royle G. *Impact of varying planning parameters on proton pencil beam scanning dose distributions in four commercial treatment planning systems*. Med Phys. 2021; 46 (3): 1150-1162.

Bertolet-Reina, A. and Carabe-Fernández, A. (2020). *Proton monoenergetic arc therapy to enhance LETd within the target*. Physics Medical and Biology, 2020 (65): 165006.

Carabe-Fernandez A, Bertolet-Reina A, Karagounis I, Huynh K, Dale RG. *Is there a role for arcing techniques in proton therapy?* Br J Radiol. (2020a); 93(1107): 20190469.

Carabe A, Karagounis IV, Huynh K, Bertolet A, François N, Kim MM, Maity A, Abel E, Dale R. *Radiobiological effectiveness difference of proton arc beams versus conventional proton and photon beams*. Phys Med Biol. (2020b) Aug 31;65(16):165002.

Caresana, M., Cirillo, A., Bolzonella, M. (Politecnico Milano). *Measurements in pulsed neutron fields.* Presentation at IM 2022 & NEUDOS 14 (2022). Kraków, 28 April 2022.

De Smet, V, De Saint-Hubert, M, Dinar, N, Manessi, GP, Aza, E, Cassell, C, Saldarriaga Vargas, C, Van Hoey, O, Mathot, G, Stichelbaut, F, De Lentdecker, G, Gerardy, I, Silari, M, Vanhavere, F. *Secondary neutrons inside a proton therapy facility: MCNPX simulations compared to measurements performed with a Bonner Sphere Spectrometer and neutron H*(10) monitors*. Radiation Measurements, (2017) Volume 992, Pages 25-40.

García-Fernández, G.F., Gallego, E., Gómez-Ros, J.M., Vega-Carrillo, H.R., Cevallos-Robalino, L.E., Guzmán-García, K.A., García-Baonza, R., Fuentes-Hernández, E. *Benchmarking of stray neutron fields produced by synchrocyclotrons and synchrotrons in compact proton therapy centers (CPTC) using MCNP6 Monte Carlo code*. Applied Radiation and Isotopes, Vol. 193 (2023), pp. 110645.

Mazal, A, Vera Sanchez JA, Sanchez-Parcerisa D, Udias JM, España S, Sanchez-Tembleque V, Fraile LM, Bragado P, Gutierrez- Uzquiza A, Gordillo N, Garcia G, Castro Novais J, Perez Moreno JM, Mayorga Ortiz L, Ilundain Idoate A, Cremades Sendino M, Ares C, Miralbell R and Schreuder N. *Biological and mechanical synergies to deal with proton therapy pitfalls: minibeams, FLASH, arcs, and gantryless Rooms*. Front. Oncol. (2021) 10: 613669.

Olsher, R.H., Seagraves, D.T., Eisele, S.L., Bjork, C.W., Martinez, W.A., Romero, L.L., Mallett, M.W., Duran, M.A., Hurlbut, C.R. *PRESCILA: A new, lightweight neutron Rem-meter*. Health Physics (2004) issue 6 p 603-612.

Paganetti, H., Beltran, C., Both, S., Dong, L., Flanz, J., Furutani, K., Grassberger, C., Grosshans, D.R., Knopf, A.C., Langendijk, J.A. *Roadmap: proton therapy physics and biology*. 2021. Phys. Med. Biol. 6605RM01.

Poirier Y, Mossahebi S, Becker SJ, Koger B, Xu J, Lamichhane N, Maxim PG, Sawant A. *Radiation shielding and safety implications following linac conversion to an electron FLASH-RT unit*. Med Phys. (2021) 48 (9): 5396-5405.

Ramoisiaux, E., Tesse, R., Hernalsteens, C., Boogert, S.T., Gnacadja, E., Nevay, L.J., Pauly, N., Shields, W., Stichelbaut, F., Vanwelde, M. *Self-consistent numerical evaluation of concrete shielding activation for proton therapy systems - Application to the proton therapy research centre in Charleroi, Belgium*. Eur. Phys. J. Plus, 137 8 (2022) 889.

Sato, T., Iwamoto, Y., Hashimoto, S., Ogawa, T., Furuta, T., Abe, S., Kai, T., Tsai, P.E., Matsuda, N., Iwase, H., Shigyo, N., Sihver, L., Niita, K. *Features of Particle and Heavy Ion Transport Code System PHITS Version 3.02*. J. Nucl. Sci. Technol. 55, 684-690 (2018).

Xiao Z, Zhang Y, Speth J, Lee E, Mascia A, Lamba M. *Evaluation of a conventionally shielded proton treatment room for FLASH radiotherapy*. Med Phys. (2022) (11): 6765-6773.

Zorloni, G. Bosmans, T. Brall, M. Caresana, M. De Saint-Hubert, C. Domingo, C. Ferrante, F. Ferrulli, R. Kopec, J. Leidner, V. Mares, R. Nabha, P. Olko, M. A. Caballero-Pacheco, W. Rühm, M. Silari, L. Stolarczyk, J. Swakon, M. Tisi, S. Trinkl, O. Van Hoey and G. Vilches-Freixas. *Joint EURADOS WG9-WG11 rem-counter intercomparison in a Mevion S250i proton therapy facility with Hyperscan pulsed synchrocyclotron*. Physics in Medicine and Biology 67, 075005 (2022a).

Zorloni, G. Bosmans, T. Brall, M. Caresana, M. De Saint-Hubert, C. Domingo, C. Ferrante, F. Ferrulli, R. Kopec, J. Leidner, V. Mares, R. Nabha, P. Olko, M. A. Caballero-Pacheco, W. Rühm, M. Silari, L. Stolarczyk, J. Swakon, M. Tisi, S. Trinkl, O. Van Hoey and G. Vilches-Freixas. *EURADOS rem counter intercomparison at Maastro proton therapy centre: comparison with literature data*. Rad. Prot. Dos. 198, 1471-1475 (2022b).

Zou W, Diffenderfer ES, Cengel KA, Kim MM, Avery S, Konzer J, Cai Y, Boisseu P, Ota K, Yin L, Wiersma R, Carlson DJ, Fan Y, Busch TM, Koumenis C, Lin A, Metz JM, Teo BK, Dong L. *Current delivery limitations of proton PBS for FLASH*. Rad. Onc. (2021); 155:212-218.

Yan, S, Lu, H.M., Flanz, J., Adams, J., Trofimov, A., Bortfeld, T. *Reassessment of the Necessity of the Proton Gantry: Analysis of Beam Orientations From 4332 Treatments at the MGH Proton Center Over the Past 10 Years*. Int J Radiat Oncol Biol Phys. (2016) 95(1): 224-233.

3.6. List of abbreviations and acronyms

CPTC	Compact Proton Therapy Centers
FBTR	Fixed Beam Treatment Room
HDR	Hourly Dose Rate
IDR	Instantaneous Dose Rate
IMPT	Intensity Modulated Proton Therapy
MU	Monitor Units
NTCP	Normal Tissue Complication Probability
PFT	Proton Flash Therapy
PMAT	Proton Monoenergetic Arc Therapy
PNFs	Pulsed neutron fields
PMB	Proton Minibeams
PRESCILA	Proton Recoil Scintillator-Los Alamos
RPTC	Roberts Proton Therapy Center
SOBP	Spread-Out Bragg Peak
TCP	Tumour Control Probability
TCR	Treatment Control Room
TR1	Technical Room 1
TI	Therapeutical Index

4. Intercomparison of radiation damage calculations in target materials at proton accelerator facilities using various Monte Carlo particle transport codes

Yosuke Iwamoto[1*], Yurdunaz Çelik [2], Francesco Cerutti[3], Robert Froeschl[3], Tommaso Lorenzon[3], Nikolai Mokhov[4], Francesc Salvat Pujol[3], Vasilis Vlachoudis[3], Lan Yao[1]

[1]Nuclear Science and Engineering Center, Japan Atomic Energy Agency, Tokai, Ibaraki, Japan

[2]Advanced Nuclear Systems Institute, SCK CEN, Belgian Nuclear Research Institute, Boeretang 200, 2400 Mol, Belgium

[3]European Organisation for Nuclear Research (CERN), Geneva, Switzerland

[4]Fermi National Accelerator Laboratory, Batavia, Illinois 60510, US

[*]iwamoto.yosuke@jaea.go.jp

In proton accelerator facilities, radiation damage calculations are necessary to evaluate its lifetime of target materials, which are exposed to the proton beam. Target lifetime evaluation relies on an assessment of energy deposition, particle (neutron, proton, pion, etc.) fluences, and Displacement Per Atom (DPA) calculations. Since benchmarking against experimental data is not possible for not directly observable physical quantities in the target, it is important to perform intercomparison among various Monte Carlo radiation-matter simulation codes, e.g. FLUKA v4-3.0, MCNP6.2 and PHITS3.26. In this work, the following four cases were selected for intercomparison of radiation damage calculations for target materials: 1) a neutron source with 30 MeV protons injected into a beryllium target, 2) a spallation neutron source at LANSCE with 800 MeV protons injected into a tungsten target, 3) a neutrino source with 30 GeV protons injected into a graphite target, and 4) an antiproton source at FNAL's pbar target station with 120 GeV protons injected into a copper target. The quantities used for the intercomparison are depth distributions of NRT-DPA (standard index of displacement damage), arc-DPA (modified index of displacement damage), deposited heat, and particle (proton, neutron, pion+, and pion-) fluence. For cases 1 and 2, the distribution of DPA was almost the same among the MC codes. On the other hand, for cases 3 and 4, the DPA values for MCNP6.2 and PHITS3.26, which consider displacement cross sections for protons and neutrons only, were smaller than those for FLUKA v4-3.0, which considers displacement cross sections for all particles, because many types of particles are produced in high-energy proton-induced nuclear reactions above 10 GeV.

4.1. Introduction

High-power proton accelerators with energies between several tens of megaelectronvolt and a few hundred gigaelectronvolt are used for the production of secondary particles from various target materials for material science, radiation therapy, and physics research. In the design and operation of accelerator facilities, it is important to assess the radiation damage in the target material, relying on physical quantities such as displacement per atom (DPA) and energy deposition, as well as particle fluences. Monte Carlo (MC) particle transport codes such as FLUKA (Ahdida *et al.*, 2022; Battistoni *et al.*, 2015) hosted by CERN, MARS (Mokhov *et al.*, 1995; Mokhov *et al.*, 2007; Mokhov *et al.*, 2014), MCNP6.2 (Goorley *et al.*, 2012), and PHITS (Sato *et al.*, 2018) are widely used to calculate these quantities in accelerator facilities. Although the same nuclear data libraries such as ENDF-B-VIII.0 (Brown *et al.*, 2018) and JENDL-4.0 (Shibata *et al.*, 2011) are used by some of the above codes, such as MCNP6.2 and PHITS, different implementation of the libraries can give different results. Moreover, the nuclear physics models adopted by the various codes (used here to perform nuclear interactions between proton and the target materials at

energies above the higher energy limit covered by nuclear data libraries) are naturally different. It is therefore essential to validate radiation-damage simulation results among various MC codes.

Radiation damage assessments are necessary to evaluate the target lifetime, requiring an evaluation of energy deposition, particle (neutron, proton, pion, etc.) fluences, and Displacement Per Atom (DPA). Since benchmarking against experimental data is not accessible for not directly observable physical quantities in the target, it is important to perform code intercomparison. In 2017, a code intercomparison of radiation damage in graphite and titanium targets under proton irradiation at various energies was performed by Mokhov *et al*. (Mokhov *et al.*, 2017). In the present contribution, four representative targets under irradiation by protons of different energies are considered (see below), with the aim of highlighting differences in the predictions of the various participating codes. The following representative target examples were considered for intercomparison of radiation damage assessments: 1) a neutron source with 30 MeV protons injected into a beryllium target, 2) a spallation neutron source at the Los Alamos Neutron Science Center (LANSCE). with 800 MeV protons injected into a tungsten target, 3) a neutrino source with 30 GeV protons injected into a graphite target, and 4) an antiproton source at pbar target station with 120 GeV protons injected into a copper target at the Fermi National Accelerator Laboratory (FNAL). The considered physical observables are energy deposition, particle fluence, and DPA in the target, scored with FLUKA v4-3.0, MCNP6.2, and PHITS3.26.

This paper is organized as follows. In section 2, a detailed description of the simulation setup is provided, as well as a succinct account of the main differences in the physics models and DPA calculation schemes among the participating codes. In Section 3, a discussion of the simulation results is provided. Finally, a summary and conclusions are provided in Section 4.

4.2. Simulation details

A succinct summary of the considered simulation scenarios is provided in Table 4.1, including the characteristics of the proton beam, as well as the dimensions and material composition of the target. Case 1 is for a neutron source with a 30 MeV proton beam impinging on a 5.5 mm thick beryllium target. Protons are fully stopped in this target. Case 2 is for a spallation neutron source with an 800 MeV proton beam impinging on a 20 cm thick tungsten target at LANSCE. Case 3 is for a neutrino source with a 30 GeV proton beam impinging on a 90 cm thick graphite target at J-PARC. Case 4 is for an antiproton source with 120 GeV proton impinging on a 20 cm thick copper target at the pbar target station at FNAL.

Table 4.1. Calculation condition with information of proton beam and target

Case	Beam	Target	Size	Density
Case 1: Neutron source with the ^{9}Be(p,n) reaction	30 MeV proton with 6 cm radius	Beryllium	5.5 mm thickness and 6 cm radius	1.85 g/cm^3
Case 2: Spallation neutron source in LANSCE	800 MeV proton with 1 cm radius	Tungsten	20 cm thickness and 1 cm radius	19.3 g/cm^3
Case 3: Neutrino source target in J-PARC	30 GeV proton with 1 cm radius	Carbon	90 cm thickness and 1 cm radius	2.2 g/cm^3
Case 4: Antiproton source target in the pbar target station at FNAL	120 GeV proton with 1 cm radius	Copper	20 cm thickness and 1 cm radius	8.96 g/cm^3

For all four cases, the following quantities are scored: fluences of proton, neutron, pion+, and pion-, energy deposition, NRT dpa (Norgett et al., 1975) and the athermal recombination correction (arc) dpa (Nordlund et al., 2018). All quantities are scored on a radius-depth mesh with one radial bin and 50 bins along the target depth.

4.2.1. Physics models in codes for this work

Figure 1 shows the physical model included in MC codes used for this work. For the FLUKA v4-3.0 calculation, the PEANUT model (Ferrari et al., 1998) is used for nuclear reactions of all hadrons from threshold energy up to 20 TeV, with the particular case of neutron reactions, accounted for in this reaction model down to 20 MeV. Below 20 MeV, instead, neutron interactions are treated in a group-wise manner for the purposes of this benchmark (note, however, that as of FLUKA v4-3.0 a point-wise treatment of low-energy neutron interactions is also available). For the MCNP6.2 calculation, nuclear reaction models, Cascade-Exciton Model (CEM) (Mashnik et al., 2008) and Los-Alamos Quark-Gluon String Model (LAQGSM) (Mashnik et al., 2008), are used for protons above 200 MeV, pions above 0.149 MeV, and neutrons above 200 MeV, respectively. The nuclear data library, JENDL-4.0/HE (Kunieda et al., 2016), is used for neutrons below 200 MeV. For the PHITS3.26 nuclear reaction models, the Liège intranuclear cascade model (INCL4.6) (Boudard et al., 2013) and Jet AA Microscopic Transportation Model (JAM) (Nara et al., 2000), are used for neutrons above 20 MeV, and protons and pions above 1 MeV, respectively. The event generator mode was applied to the neutron incident reaction below 20 MeV.

Figure 1. Physics models in MC codes used in this work

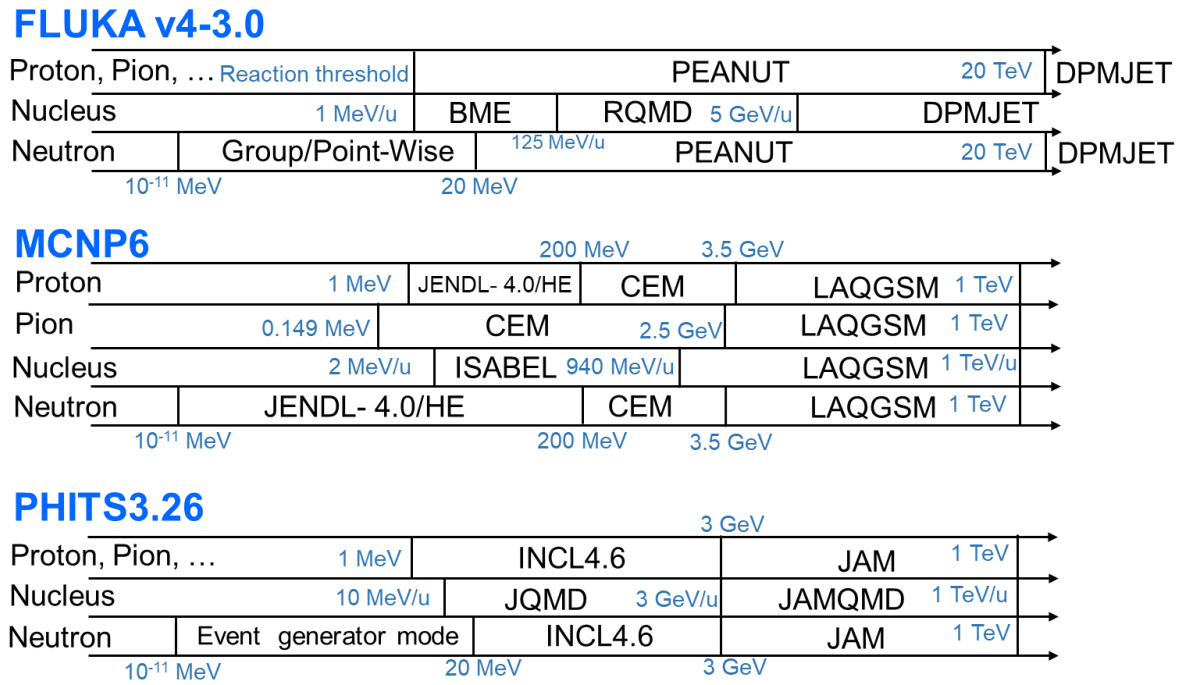

4.2.2. DPA calculation method

The displacement cross section is determined by the number of atomic displacements as shown below:

$$\mathbf{DPA} = \int \sigma_{\mathrm{disp}}(E)\, \emptyset(E) dE$$

$$N_{\mathrm{NRT}}(T_{\mathrm{d}}) = \begin{cases} 0\ , & T_{\mathrm{d}} < E_{\mathrm{d}} \\ 1\ , & E_{\mathrm{d}} < T_{\mathrm{d}} < \dfrac{2E_{\mathrm{d}}}{0.8} \\ \dfrac{0.8}{2E_{\mathrm{d}}} T_{\mathrm{d}}, & \dfrac{2E_{\mathrm{d}}}{0.8} < T_{\mathrm{d}} < \infty \end{cases}$$

where σ_{disp} is the displacement cross section of the incident particle, E is the kinetic energy of the incident particle, $\emptyset$ is the particle fluence, T_{d} is the damage energy, and E_{d} is the displacement energy in a material. In the NRT model developed in 1975 (Norgett *et al.*, 1975), the atomic displacement number, N_{NRT}, was the ratio of the damage energy transferred to a lattice atom to the threshold energy. In 2018, a new method, the athermal recombination corrected (arc) DPA model, based on Molecular Dynamics simulations was proposed (Nordlund *et al.*, 2018). The arc model proposes the defect production efficiency as a function of damage energy as shown below:

$$N_{\mathrm{arc}}(T_{\mathrm{d}}) = \begin{cases} 0\ , & T_{\mathrm{d}} < E_{\mathrm{d}} \\ 1\ , & E_{\mathrm{d}} < T_{\mathrm{d}} < \dfrac{2E_{\mathrm{d}}}{0.8} \\ \dfrac{0.8T_{\mathrm{d}}}{2E_{\mathrm{d}}} \zeta_{arc}(T_{\mathrm{d}}), & \dfrac{2E_{\mathrm{d}}}{0.8} < T_{\mathrm{d}} < \infty \end{cases}$$

$$\zeta_{arc}(T_{\mathrm{d}}) = \frac{1 - c_{\mathrm{arcdpa}}}{(2\,E_{\mathrm{d}}/0.8)^{b_{\mathrm{arcdpa}}}} T_{\mathrm{d}}^{b_{\mathrm{arcdpa}}} + c_{\mathrm{arcdpa}}$$

where b_{arcdpa}, c_{arcdpa}, and E_{d}, threshold damage energy, are material-dependent parameters. Table 4.2 summarizes material-dependent parameters for displacement cross sections used in this work. For FLUKA v4-3.0 and PHITS3.26, material-dependent parameters were obtained from references (Iwamoto et al. 2020; Konobeyev et al. 2017).

Table 4.2. Material-dependent parameters for displacement cross sections used in this work

	Be, Case 1	W, Case 2	C, Case 3	Cu, Case 4
b_{arcdpa}	-1 for FLUKA v4-3.0 and PHITS3.26	-0.56 for FLUKA v4-3.0 and PHITS3.26 -0.564 for MCNP6.2	-1 for FLUKA v4-3.0 and PHITS3.26	-0.68 for all
c_{arcdpa}	0.46 for FLUKA v4-3.0 and PHITS3.26	0.12 for FLUKA v4-3.0 and PHITS3.26 0.119 for MCNP6.2	0.710 for FLUKA v4-3.0 and PHITS3.26	0.16 for all
E_{d}	31 eV for FLUKA v4-3.0 and PHITS3.26 31.19 eV for MCNP6.2	70 eV for all	69 eV for FLUKA v4-3.0 and PHITS3.26 69.28 eV for MCNP6.2	33 eV for FLUKA v4-3.0 and PHITS3.26 30 eV for MCNP6.2

Note: The parameters of b_{arcdpa} and c_{arcdpa} for displacement cross sections used in MCNP6.2 are not indicated.

The NRT- and arc- displacement cross sections calculated with FLUKA v4-3.0 and PHITS3.26 were employed in the radiation damage calculations using the respective codes. All material-dependent parameters used in each MC code are almost same. Note that NRT- and arc- displacement cross sections used in MCNP6.2 are taken from the displacement cross section data based on the reference (Konobeyev et al. 2018). Since the maximum

energy of incident particle is 10 GeV for the displacement cross section (Konobeyev et al. 2018), the displacement cross sections for particles with energies of 10 GeV were used for those above 10 GeV. DPA is calculated with MCNP6.2 code by folding displacement cross section with particle spectrum. The b_{arcdpa} and c_{arcdpa} parameters for the displacement cross sections used in MCNP6.2 are not shown in Table 4.2 due to lack of information in (Konobeyev et al. 2018). Calculations with MCNP6.2 and PHITS3.26 include displacement cross section of proton and neutron only. FLUKA v4-3.0 calculations include displacement cross section of all particles.

4.3. Results and discussion

Radiation damage distributions in depth in the target were calculated for all cases listed in Table 4.1. The calculated radiation damage includes NRT-dpa, arc-dpa, thermal, proton fluence, and neutron fluence. Except for case 1, pion+ and pion- fluences are included.

Figure 4.2. Radiation damage distribution for 30 MeV proton on a 0.6 cm thick Be target

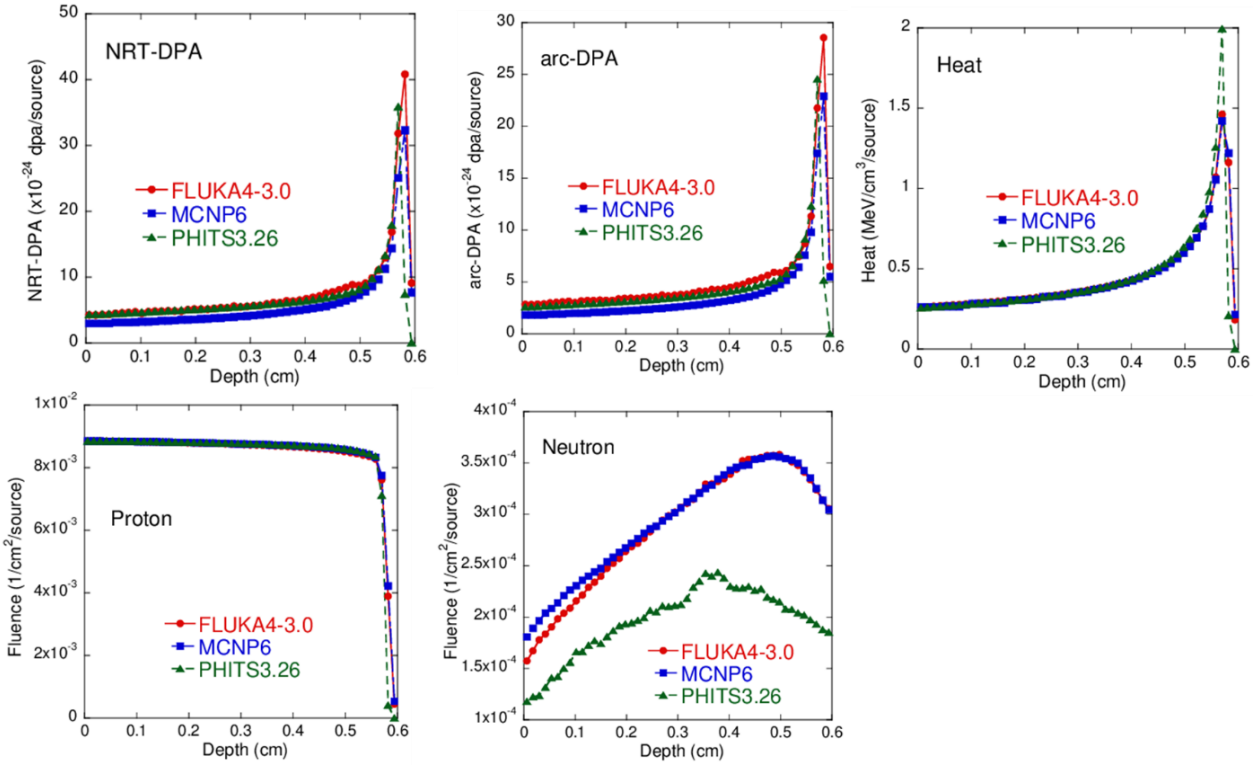

Figure 4.2 displays the depth distribution of the aforementioned observables in a beryllium target during 30 MeV proton incidence. The 30 MeV protons stop completely within this target, resulting in the appearance of a Bragg peak in the energy deposition distribution. Between codes, all calculated results were in general agreement within a factor of 2. For neutron fluence, PHITS3.26 was lower than FLUKA v4-3.0 and MCNP6.2 by a factor of 1.8. PHITS performs the ^{9}Be(p,xn) nuclear reaction with the intra nuclear cascade model and the evaporation model. This difference is due to the treatment of ^{9}Be(p,xn) nuclear reactions in each physics model of the FLUKA and PHITS. It can be seen that fewer neutrons are produced by INCL4.6 in PHITS3.26 than by PEANUT in FLUKA v4-3.0 or JENDL library used in MCNP6.2. As for the heat results, the Bragg peaks calculated by

PHITS3.26 are sharper than the others. The model of energy and angular straggling of protons in the target of PHITS3.26 is different from that of FLUKA v4-3.0 and MCNP6.2.

Figure 4.3. Radiation damage distribution for 800 MeV proton on a 20 cm thick W target

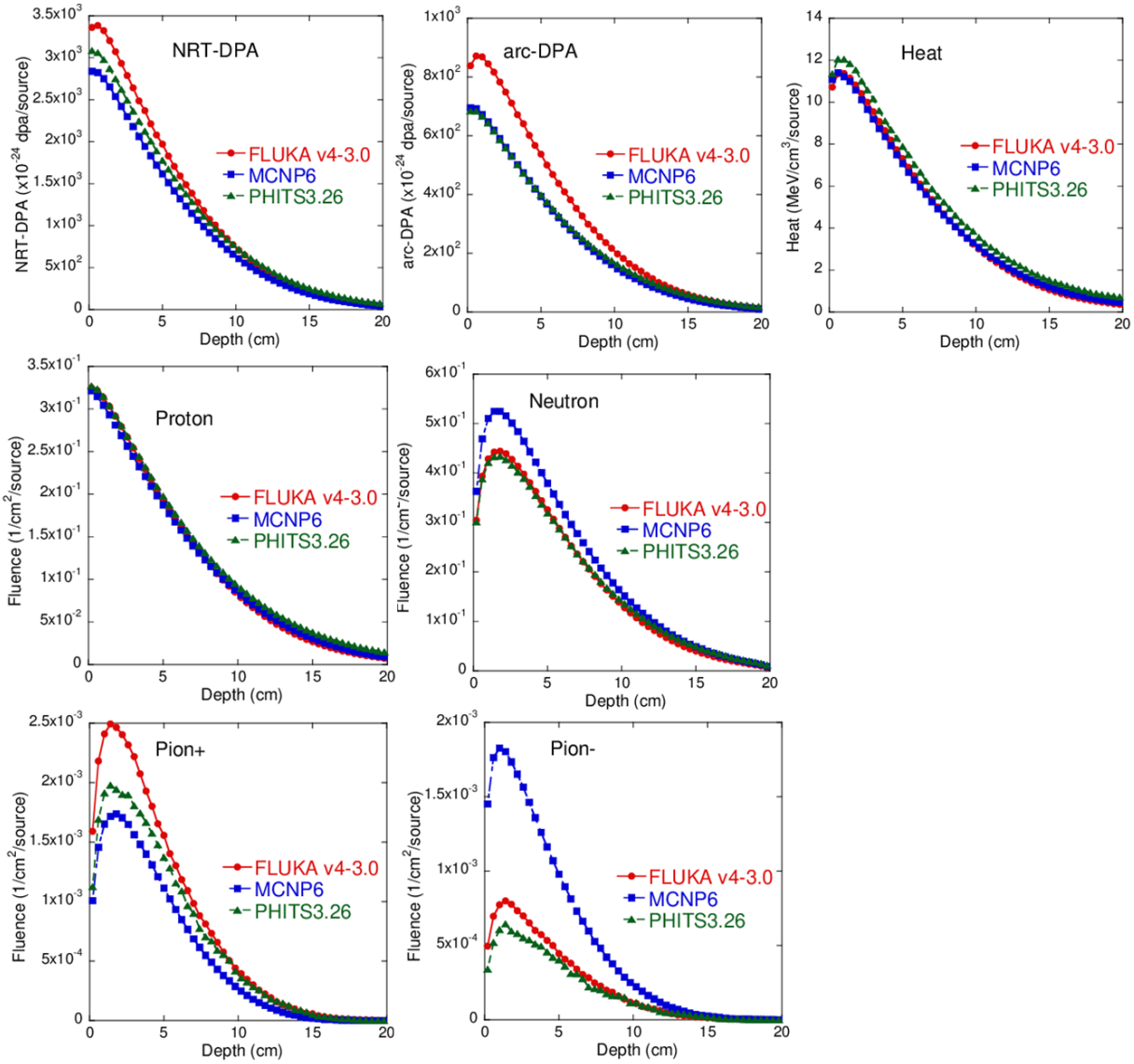

Figure 4.3 displays the depth distribution of the aforementioned observables in a tungsten target for 800 MeV proton incidence. All results agree within a factor of 2 among codes, except for the pion- fluence. The pion- fluence calculated by MCNP6.2 is about three times larger than that of FLUKA v4-3.0 and PHITS3.26. As the energy of the incident proton increases, the number of pions increases due to high energy nuclear reactions. The difference in pion fluence is attributed to the difference in nuclear reaction models. In NRT-DPA and arc-DPA, FLUKA v4-3.0 results are higher than the other codes, even though FLUKA v4-3.0 has the same proton and neutron fluence as the other codes; the difference in DPA between MC codes is attributed to the difference in proton and neutron displacement cross sections used in each MC code.

Figure 4.4. Radiation damage distribution for 30 GeV proton on a 90 cm thick Graphite

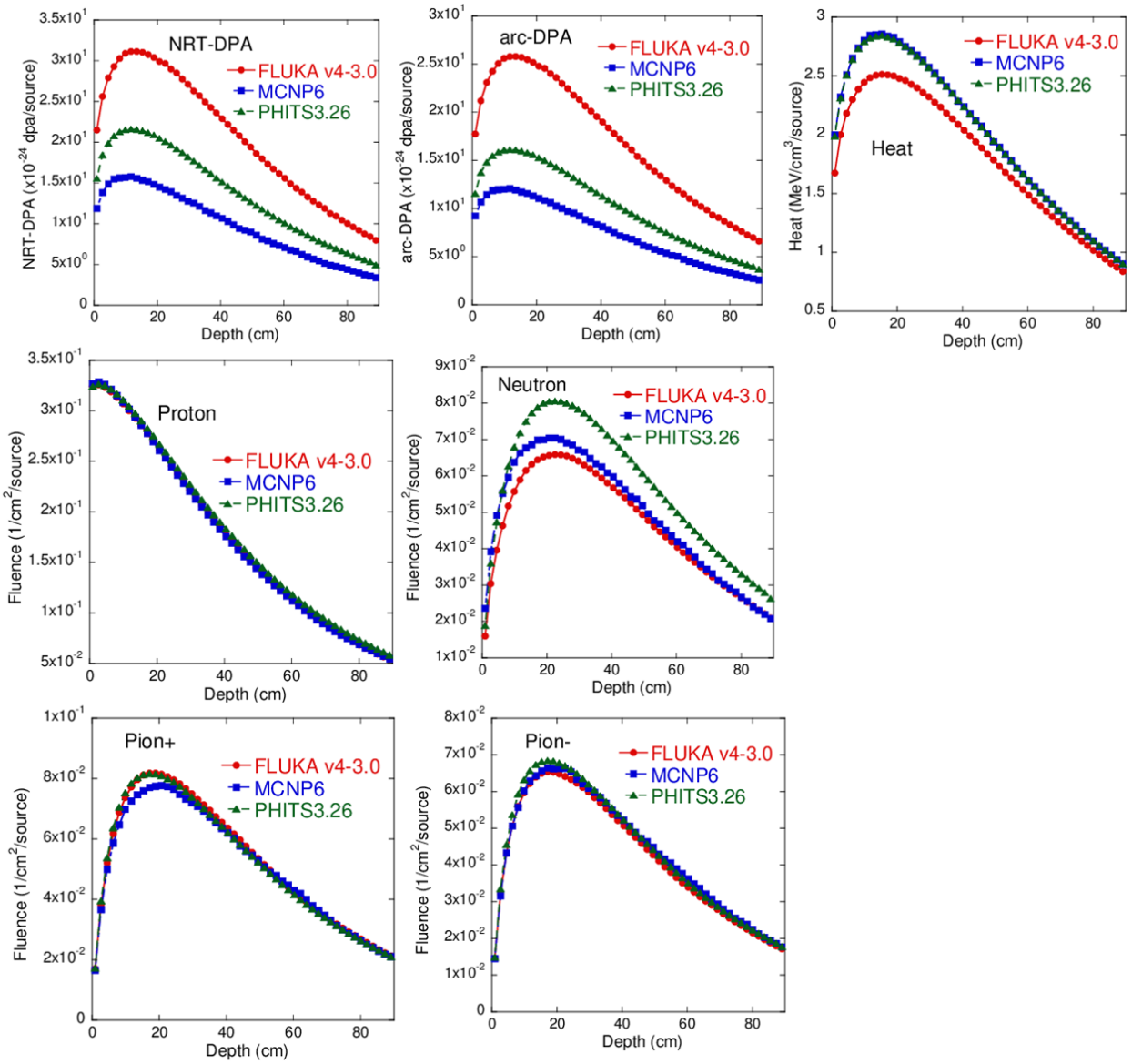

Figure 4.4 displays the depth distribution of the aforementioned observables in a graphite target for 30 GeV proton incidence. The results, except for the distribution of DPA, are consistent within a factor of 2 among MC codes. On the other hand, the calculation of DPA differs among MC codes. The difference in DPA between MCNP6.2 and PHITS3.26 is due to the difference in neutron fluence when the displacement cross section used in MCNP6.2 is the same as in PHITS3.26. The DPAs calculated with FLUKA v4-3.0 are larger than the others even though the neutron fluence calculated with FLUKA v4-3.0 is lower than the others. This is due to the fact that the MCNP6.2 and PHITS3.26 calculations includes displacement cross sections for protons and neutrons only, whereas the FLUKA4-3.0 calculation includes displacement cross sections for all particles. A comparison of Figures 4.3 and 4.4 shows that the higher the proton energy, the larger the contribution of particles other than protons and neutrons, resulting in a larger difference in DPA.

Figure 4.5. Radiation damage distribution for 120 GeV proton on a 20 cm thick copper

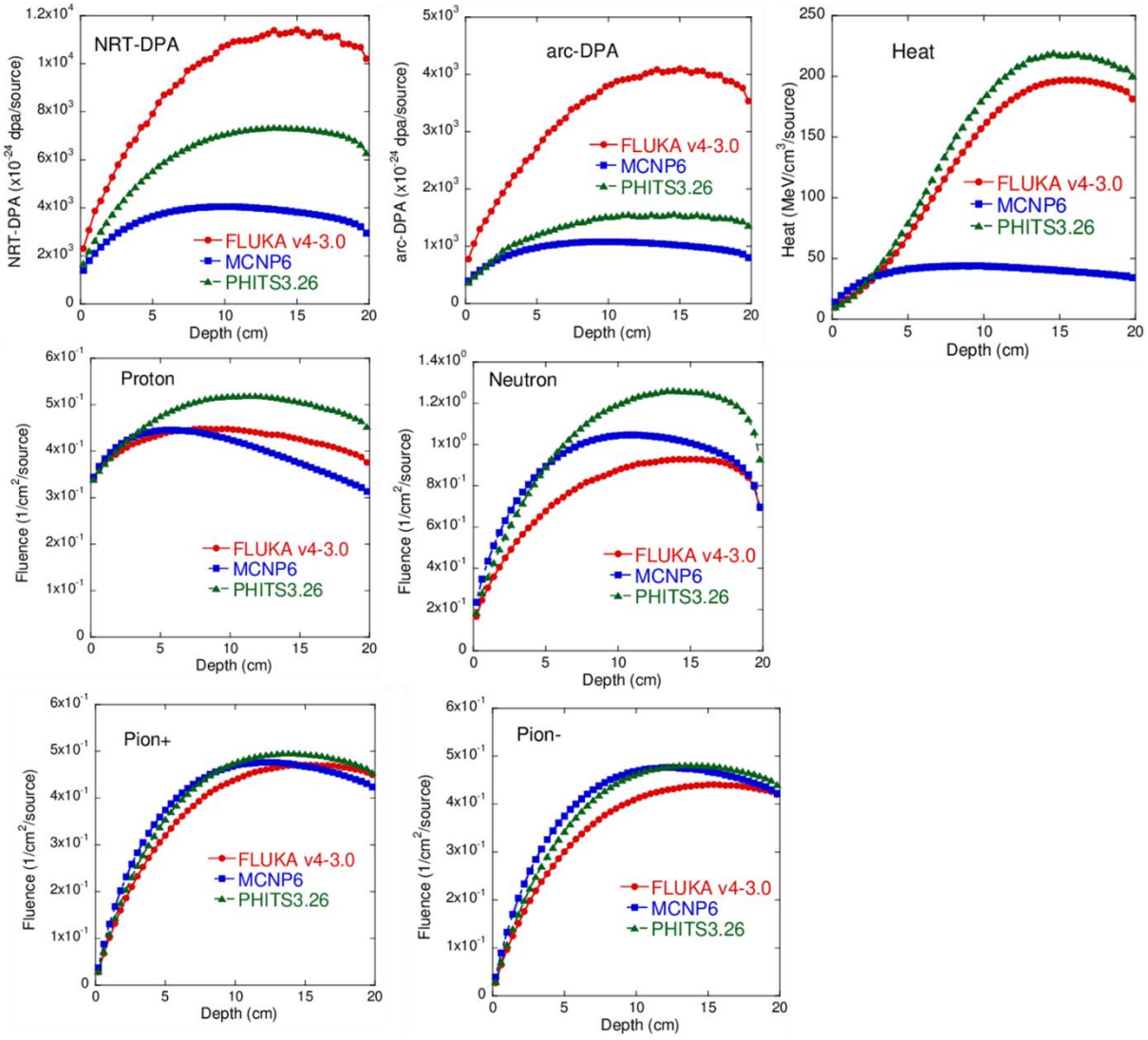

Figure 4.5 displays the depth distribution of the aforementioned observables in the copper target for 120 GeV proton incidence. The proton and neutron fluence results differ between codes because the hadron shower production process in copper during 120 GeV proton irradiation depends on the physical model used. The relationship of DPA with FLUKA4-3.0, MCNP6.2, and PHITS3.26 are similar with those in Figure 4.4. For Heat, MCNP6.2 is lower than FLUKA4-3.0 and PHITS3.26 by a factor of around 5. Even though all possible secondary particles are transported during MCNP6.2 calculations, obtained total heating values for this high energy are somehow wrongly calculated. MCNP developer team has been informed and investigation is still ongoing.

In the future, we will compare the proton and neutron displacement cross sections used in each MC code to determine the differences in the DPA distributions in all cases. We will also investigate the contribution of other particles such as pions, gamma-rays, and electrons to the DPA distribution for the 30 GeV and 120 GeV proton incident cases.

4.4. Summary

Intercomparison of radiation damage calculations for target materials using FLUKA v4-3.0, MCNP6.2, and PHITS3.26 was performed for the following four cases: 1) a neutron source with 30 MeV protons injected into a beryllium target, 2) a spallation neutron source with 800 MeV protons injected into a tungsten target at LANSCE, 3) neutrino source with 30 GeV protons injected into a graphite target, and 4) antiproton source with 120 GeV protons impinging on a copper target at the FNAL pbar target station. The quantities used for intercomparison are the depth profiles of NRT-DPA, arc-DPA, heat, and particle fluence for protons, neutrons, pion+, and pion-. For cases 3 and 4, the differences between the codes for particle fluence and heat increased with increasing incident proton energy. For cases 1 and 2, the distribution of DPA was almost the same among the MC codes. On the other hand, for cases 3 and 4, it is clear that the DPA values for MCNP6.2 and PHITS3.26, which consider only proton and neutron cross sections, are smaller than those for FLUKA v4-3.0, which consider cross sections for all particles, because many types of particles are produced in high-energy proton-induced nuclear reactions above 10 GeV. Future work will include a comparison of the displacement cross sections used in the codes.

4.5. Acknowledgements

This work was supported in part by Japan Society for the Promotion of Science (JSPS) Grant-in-Aid for Scientific Research (KAKENHI) Grant Number 19H02652.

4.6. List of references

Ahdida, C., Bozzato, D., Calzolari, D., Cerutti, F., Charitonidis, N., Cimmino, A., Coronetti, A., D'Alessandro, G. L. , Donadon Servelle, A., Esposito, L. S., Froeschl, R., Garcia Alia, R., Gerbershagen, A., Gilardoni, S., Horvath, D., Hugo, G., Infantino, A., Kouskoura, V., Lechner, A., Lefebvre, B., Lerner, G., Magistris, M., Manousos, A., Moryc, G., Ogallar Ruiz, F., Pozzi, F., Prelipcean, D., Roesler, S., Rossi, R., Sabate Gilarte, M., Salvat Pujol, F., Schoofs, P., Stransky, V., Theis, C., Tsinganis, A., Versaci, R., Vlachoudis, V., Waets, A. and Widorski, M. (2022), "New Capabilities of the FLUKA Multi-Purpose Code", *Frontiers in Physics*, 9, 788253.

Battistoni, G., Boehlen, T., Cerutti, F., Chin, P.W., Esposito, L.S., Fasso, A., Ferrari, A., Lechner, A., Empl, A., Mairani, A., Mereghetti, A., Garcia Ortega, P., Ranft, J., Roesler,, S., Sala, P.R., Vlachoudis, V., Smirnov, G. (2015), "Overview of the FLUKA code", *Annals of Nuclear Energy* 82, 10-18.

Boudard, A., Cugnon, J., and David, J.C. (2013), "New potentialities of the Liège intranuclear cascade model for reactions induced by nucleons and light charged particles", Phys. Rev. C 87, 014606.

Brown, D.A., Chadwick, M.B., Capote, R., Kahler, A.C., Trkov, A., Herman, M.W., et al. (2018), "ENDF/B-VIII.0: The 8th Major Release of the Nuclear Reaction Data Library with CIELO-project Cross Sections, New Standards and Thermal Scattering Data", *Nuclear Data Sheets*, 148, 1-142.

Ferrari, A. and Sala P. (1998), "The Physics of High Energy Reactions", Proceedings Workshop on Nuclear Reaction Data and Nuclear Reactor Physics, Design, and Safety, World Scientific.

Goorley, T. et al. (2012), "Initial MCNP6.2 release overview", *Nucl. Technol.*, 180, pp. 298-315.

Iwamoto, Y., Meigo, S.I. and Hashimoto, S. (2020), “Estimation of reliable displacements-per-atom based on athermal-recombination-corrected model in radiation environments at nuclear fission, fusion, and accelerator facilities”, Journal of Nuclear Materials 538, 152261.

Konobeyev, A.Yu., Fischer, U. Korovin, Yu. A., and Simakov, S.P., (2017) “Evaluation of effective threshold displacement energies and other data required for the calculation of advanced atomic displacement cross-sections”, Nuclear Energy and Technology 3, 169-175.

Konobeyev, A.Yu., Fischer, U. and Simakov, S.P., (2018) “Improved atomic displacement cross-sections for proton irradiation of aluminium, iron, copper, and tungsten at energies up to 10 GeV”, Nucl. Instrum. Meth. B 431, 55-58, https://www-nds.iaea.org/public/download-endf/DXS/Displacement_XS/DXS.(2018)/.

Kunieda, S., et al. (2016), “Overview of JENDL-4.0/HE and benchmark calculation”, JAEA-Conf 2016-004, 41-46.

Mashnik, S.G., Gudima, K.K., Prael, R.E., Sierk, A.J., Baznat, M.I. and Mokhov, N.V. (2008), “CEM03.03 and LAQGSM03.03 event generators for the MCNP6, MCNPX, and MARS15 transport codes”, LANL Report LAUR-08-2931, Los Alamos; arXiv:0805.0751.

Mokhov, N.V. and S.I. Striganov (2007), MARS15 Overview, AIP Conference Proceedings 896, pp. 50-60, United States, https://doi.org/10.1063/1.2720456.

Mokhov, N.V. et al. (1995), “The MARS Code System User’s Guide”, Fermilab-FN-628.

Mokhov, N.V., P. Aarnio, Yu. Eidelman, K. Gudima, A. Konobeev, V. Pronskikh, I. Rakhno, S. Striganov and I. Tropin (2014), “MARS15 code developments driven by the Intensity Frontier needs”, Prog. Nucl. Sci. Tech., 4, pp. 496-501.

Mokhov, N.V. et al. (2017), “Code Inter-Comparison for Radiation Damage Related Quantities”, NBI2017+RaDIATE IVIL, Tokai, Japan, September 18-22, 2017.

Nara, Y., H. Otuka, A. Ohnishi, et al. (2000), “Relativistic nuclear collisions at 10A GeV energies from p+Be to Au+Au with the hadronic cascade model”, Phys. Rev. C 61, 024901.

Nordlund, K. et al. (2018), “Improving atomic displacement and replacement calculations with physically realistic damage models”, Nature Communications, 9, pp. 1084.

Norgett, M.J., Robinson, M.T. and Torrens, I. M. (1975), “A proposed Method of Calculating Displacement Dose Rates”, Nucl. Engineering and Design, 33, pp. 50-54.

Sato, T. et al. (2018), “Features of particle and heavy ion transport code system (PHITS) version 3.02”, *J. Nucl. Sci. Technol.*, 55[12], pp. 529-533.

Shibata, K., Iwamoto, O., Nakagawa, T., Iwamoto, N., Ichihara, A., Kunieda, S., et al. (2011), “JENDL-4.0: A New Library for Nuclear Science and Engineering”, *J. Nucl. Sci. Technol.*, 48 [1], pp. 1-30.

5. Shielding at high-power, high-intensity laser facilities: source term assessment for HED science and the Athena Lab for medical applications at HZDR

Anna Ferrari, Thomas E. Cowan, Lingen Huang, Josefine Metzkes-Ng, Stephan Kraft
Helmholtz-Zentrum Dresden-Rossendorf
Corresponding Author(s): ronninge@msu.edu

Physics of high power, ultra-intense lasers interacting with plasma is a field that dramatically evolved in the last years, with a growing number of multi-TW and PW-class dedicated facilities around the world. In a such scenario an optimized shielding assessment still appears to be a challenge: if on one hand the constant technological improvements are allowing increased energies and intensities of the emitted ionizing radiation, on the other hand some aspects of the underlying physical phenomena still need more investigation.

In this work the shielding concept for two different, complex laser-induced radiation fields will be presented, as significant cases:
(1) After accurate investigation of the dynamics of hot refluxing electrons in the interaction of an ultra-short relativistic laser pulse with a thin foil target via particle-in-cell (PIC) simulations, and comparison with experimental data, the typical Bremsstrahlung source term has been evaluated, taking into account for the first time the photon radiation emitted from the recirculating electrons in the plasma. This source term primarily drives the radiation protection assessment in the facilities dedicated to the investigation of the matter under extreme conditions.

(2) The shielding concept of the ATHENA Lab, which is at present in construction at HZDR and will use the PENELOPE PW laser for biology and medical applications, will be presented. The shielding assessment has been realized considering two different operation modes: (a) a 'full energy' mode, where we assume that the full energy spectrum of interest for the biology/medical applications (up to 250 MeV) is reached via advanced acceleration schemes; (b) a 'routine operation' mode, with a lower, stable working point as maximum proton energy (100 MeV). The data-driven source terms used, together with the optimization process, will be described and discussed.

6. Solid state dosimeters at Laser-Driven Accelerator Facilities

Anna Cimmino[1], Dávid Horváth[1], Veronika Olšovcová[1], Carlo Maria Lazzarini[1], Gabriele Maria Grittani[1], Iva Ambrožová[2], Zeljka Knezevic[3], Marija Majer[3]
[1] ELI Beamlines
[2] Nuclear Physics Institute of the CAS
[3] Institut Ruđer Bošković
Corresponding Author(s): anna.cimmino@eli-beams.eu

Over the past few decades, laser-based particle accelerators have made tremendous progress and attracted ever more interest from the wider scientific community. Multiterawatt and petawatt highpower lasers facilities are now a reality and have applications in physics, material science, medicine, life science, and laboratory astrophysics. The radiation generated in experiments using such laser systems leads to high prompt doses and potentially to the activation of the surrounding materials. Unfortunately, in comparison with conventional accelerators, accurate dosimetry at laser-accelerated beams is still a challenge. The radiation fields produced are pulsed, mixed, and with high instantaneous fluxes and high dose rates. While new dosimetric techniques are being developed, important efforts are being put in the study of the behavior of known dosimetry systems in radiation fields at laser accelerators.

This work presents a study of passive solid-state detectors for the measurement of pulsed radiation performed at experimental station ALFA. ALFA was commissioned at the ELI Beamlines laser driven user facility. Laser pulses (<20 fs, 1kHz, 1.5 TW) were carefully focused inside supersonic gas targets to generate an ultra-short (fs) ultra-relativistic (10s MeV) electron beam. The produced secondary radiation field was studied and has provided useful insights in dosimetry at laser accelerator. To achieve better understanding, a combination of different solid-state dosimetric systems were irradiated: film badges and optically stimulated luminescence, thermoluminesce, and radiophotoluminescence dosimeters. Furthermore, detailed Monte Carlo simulations were performed. This contribution presents the obtained experimental data and their comparison to Monte Carlo predictions.

7. A new methodology for plugging of pipe/cable penetrations in shielding walls for gamma and neutron radiation

Ralf Buckermann, Lars Ackermann
Framatome GmbH, Erlangen, GERMANY
ralf.buckermann@framatome.com

In the frame work of shielding design for the OL3 nuclear power plant (NPP) a special design solution was required to shield the areas close to the circular wall inside the Reactor Building.

In the Reactor Building of the OL3 NPP, large equipment areas with high neutron and gamma radiation levels are separated from accessible areas by one circular shielding wall comprising the Reactor Coolant System. This shielding wall is penetrated by a large number of openings for cables and piping of different diameters and temperature requirements. The openings are generally realized during the construction phase by using sleeve pipes in the first concreting of the shielding wall.

These openings may be used by a single pipe as well as by different pipes routed through the opening at different angles. The installation of the piping has generally to include enough flexibility to allow moving of the piping due to thermal stress and other possible impacts. Furthermore, the installation of the piping shall include the option to remove and exchange piping during plant outage. These openings have to be sealed according to the radiological requirements of very low radiation levels given for the accessible areas. This was quite demanding taking into account the huge impact induced by the Reactor Coolant System in the large equipment areas.

After the sleeving – a very common standard technique - of each pipe (in some cases sleeving of pipes of small bore as a bundle) to allow enough flexibility after installation, the opening is filled with PE granules. This was done by a commonly used fan systems conveying the granules into the openings. These PE granules yield good neutron attenuation due to their high hydrogen content. Lead wool packages (used for OL3, comparable gamma attenuation materials can be used instead) were introduced in the openings at both ends to shield any gamma radiation impact.

The complete design yielded enough space to add additional sealing for room closure (HVAC) and fire protection sealing as final steps of the overall sealing procedure. The sealing procedure is quickly performed. The preparatory works as well as the impact on the areas around are quite low. The seals can easily be removed for exchange or addition of pipes etc.

It is shown on examples that the implementation method for the PE granules into the opening yielded a density that was high enough to provide sufficient neutron radiation attenuation. Calculations by Monte Carlo particle transport code, MCNP, showed that the total radiation dose rate attenuation of the complete seal is as good as of the unpenetrated wall. Radiological measurements during plant start-up measurements at OL3 at 60 % reactor power (commissioning of the plant and further increase of the reactor power is still ongoing) demonstrated in April that the neutron and gamma radiation dose rate levels at these openings are kept. According to the measurement results it can already be stated that the dose rates at these plugged openings will remain at the predicted low levels when reaching 100% reactor power. The patent applications for the plugging methodology are in progress. It is available under its Framatome product name "Flexible Radiation Plugging – Flex Rad Plug".

8. Atmospheric-like neutrons and muons at the ILC beam dumps

Yasuhito Sakaki, Shinichiro Michizono. Nobuhiro Terunuma, Toshiya Sanami
KEK
Corresponding Author(s): sakakiy@post.kek.jp

We evaluate the neutron and muon fluxes produced in the ILC beam dump by Monte Carlo simulations and discuss their potential use in irradiation fields. We find that the beam dumps can deliver neutrons about 10^{11} times the cosmic radiation on spaces perpendicular to the beam axis and muons times downstream of the beam dumps in the initial phase of the ILC. Large-area irradiation of the order of 1 m2 or more is possible. Differences in the energy distribution of muons in electron and positron beam dumps are also discussed.